



HAL
open science

Malvinas current at 44.7°S: First assessment of velocity temporal variability from in situ data

Guillermina Fernanda Paniagua, Martin Saraceno, Alberto R. Piola, Marcela Charo, Ramiro Ferrari, Camila Artana, Christine Provost

► To cite this version:

Guillermina Fernanda Paniagua, Martin Saraceno, Alberto R. Piola, Marcela Charo, Ramiro Ferrari, et al.. Malvinas current at 44.7°S: First assessment of velocity temporal variability from in situ data. Progress in Oceanography, 2021, 195, pp.102592. 10.1016/j.pocean.2021.102592 . hal-03380811

HAL Id: hal-03380811

<https://cnrs.hal.science/hal-03380811v1>

Submitted on 15 Oct 2021

HAL is a multi-disciplinary open access archive for the deposit and dissemination of scientific research documents, whether they are published or not. The documents may come from teaching and research institutions in France or abroad, or from public or private research centers.

L'archive ouverte pluridisciplinaire **HAL**, est destinée au dépôt et à la diffusion de documents scientifiques de niveau recherche, publiés ou non, émanant des établissements d'enseignement et de recherche français ou étrangers, des laboratoires publics ou privés.

Progress in Oceanography

Malvinas Current at 44.7°S: First assessment of velocity temporal variability from in situ data

--Manuscript Draft--

Manuscript Number:	
Article Type:	Full Length Article
Section/Category:	Physical and Geophysical Oceanography
Keywords:	MALVINAS CURRENT VARIABILITY; IN SITU TIME SERIES; ALTIMETRY DATA; PATAGONIAN SLOPE
Corresponding Author:	Guillermina Fernanda Paniagua, PhD Student CIMA: Centro de Investigaciones del Mar y la Atmosfera ARGENTINA
First Author:	Guillermina Fernanda Paniagua, PhD Student
Order of Authors:	Guillermina Fernanda Paniagua, PhD Student Martin Saraceno Alberto R. Piola Marcela Charo Ramiro Ferrari Camila Artana Christine Provost
Abstract:	<p>Abstract</p> <p>We report current meter measurements obtained by four moorings deployed across the Malvinas Current (MC) at 44.7°S during 18 months between December 2015-June 2017. Previous measurements of the MC strength have been reported only close to the Brazil-Malvinas Confluence, hindering the interpretation of the flow variability. The record-length time averaged velocities and variance ellipses indicate a strong northward along-isobath flow with an equivalent-barotropic structure. The meridional velocities at the western and eastern moorings are not correlated and show large amplitude oscillations which are coherent with the passage of mesoscale features over the moorings. Satellite altimetry data, that are highly correlated with 20-day low-pass filtered in situ velocities ($r \sim 0.80$), show that the MC variability is affected by the propagation of sea level anomalies (SLA) along the Patagonian slope with phase speeds that range between $0.21 \pm 0.04 \text{ m s}^{-1}$ and $0.14 \pm 0.01 \text{ m s}^{-1}$. SLAs propagate northward along the slope following contours of constant potential vorticity and its phase speeds decrease towards the east across the slope. SLAs that mostly affect the western mooring originate in the northern flank of the North Scotia Ridge while SLAs that mostly affect the eastern mooring originate along the Malvinas Escarpment, along the northern edge of the Malvinas Plateau. We suggest that the interaction between eddies and the complex bathymetry at those locations generate instabilities that enhance the generation of mesoscale structures that propagate in the flow direction along the western boundary of the Argentine Basin affecting the variability of the MC velocities.</p>
Suggested Reviewers:	<p>Magdalena Carranza magdalena@mbari.org</p> <p>Antonio Fetter antonio.fetter@ufpe.br</p> <p>Matthieu Le Hénaff m.lehenaфф@miami.edu</p>
Opposed Reviewers:	

1
2
3
4 **1 Malvinas Current at 44.7°S: First assessment of velocity temporal variability**
5
6 **2 from in situ data**
7
8
9 **3**

10 **4 Guillermina F. Paniagua^{1,2,3}, Martin Saraceno^{1,2,3}, Alberto R. Piola^{2,3,5}, Marcela Charo⁵,**
11 **5 Ramiro Ferrari^{1,2,3}, Camila Artana⁶ and Christine Provost⁴**
12
13
14 **6**

15
16 ¹ Centro de Investigaciones del Mar y la Atmósfera (CIMA/CONICET-UBA), Ciudad Autónoma
17 de Buenos Aires, Argentina
18

19
20 ² Departamento de Ciencias de la Atmósfera y los Océanos, Facultad de Ciencias Exactas y
21 Naturales, Universidad de Buenos Aires, Buenos Aires, Argentina
22

23
24 ³ Unidad Mixta Internacional-Instituto Franco-Argentino para el Estudio del Clima y sus
25 Impactos (UMI-IFAECI/CNRS-CONICET-UBA), Buenos Aires, Argentina
26

27
28 ⁴ Laboratoire d'Océanographie et du Climat: Experimentation et Approches Numériques
29 (LOCEAN), UMR 7159, Paris, Francia
30

31
32
33 ⁵ Departamento de Oceanografía, Servicio de Hidrografía Naval (SHN), Buenos Aires, Argentina
34

35 ⁶ MERCATOR OCEAN, Parc Technologique du Canal, Ramonville Saint Agne, France
36
37

38
39 Corresponding author: Guillermina F. Paniagua (guillermina.paniagua@cima.fcen.uba.ar)
40
41

42 **19 Highlights:**
43

- 44
45 **20** • Up to 18-months of in situ current data were obtained at 44.7°S at different depths within
46 the Malvinas Current.
47
48
49 **22** • The easternmost and westernmost meridional velocities are not correlated due to the
50 presence of mesoscale features in the Malvinas Current.
51
52
53 **24** • A large oscillation with a periodicity of about 40 days is observed in the meridional velocity
54 measurements.
55
56

57 **26**
58
59
60
61
62
63
64
65

Abstract

We report current meter measurements obtained by four moorings deployed across the Malvinas Current (MC) at 44.7°S during 18 months between December 2015-June 2017. Previous measurements of the MC strength have been reported only close to the Brazil-Malvinas Confluence, hindering the interpretation of the flow variability. The record-length time averaged velocities and variance ellipses indicate a strong northward along-isobath flow with an equivalent-barotropic structure. The meridional velocities at the western and eastern moorings are not correlated and show large amplitude oscillations which are coherent with the passage of mesoscale features over the moorings. Satellite altimetry data, that are highly correlated with 20-day low-pass filtered in situ velocities ($r \sim 0.80$), show that the MC variability is affected by the propagation of sea level anomalies (SLA) along the Patagonian slope with phase speeds that range between $0.21 \pm 0.04 \text{ m s}^{-1}$ and $0.14 \pm 0.01 \text{ m s}^{-1}$. SLAs propagate northward along the slope following contours of constant potential vorticity and its phase speeds decrease towards the east across the slope. SLAs that mostly affect the western mooring originate in the northern flank of the North Scotia Ridge while SLAs that mostly affect the eastern mooring originate along the Malvinas Escarpment, along the northern edge of the Malvinas Plateau. We suggest that the interaction between eddies and the complex bathymetry at those locations generate instabilities that enhance the generation of mesoscale structures that propagate in the flow direction along the western boundary of the Argentine Basin affecting the variability of the MC velocities.

Keywords

- MALVINAS CURRENT VARIABILITY
- IN SITU TIME SERIES
- ALTIMETRY DATA
- PATAGONIAN SLOPE

1. Introduction

The Malvinas Current (MC) originates as a branch of the Antarctic Circumpolar Current (Peterson and Whitworth, 1989; Piola and Gordon, 1989) veering northward approximately following the path of the Subantarctic Front into the western Argentine Basin. Reaching 38°S, the MC causes the northernmost penetration of subpolar waters in the southern hemisphere. Thus, it contributes to the meridional heat transport and to regulate the climate on Earth (Garzoli and Matano, 2011). In situ current measurements have been collected mostly at 40-41°S (Vivier and Provost, 1999a; 1999b; Spadone and Provost, 2009; Ferrari et al., 2017; Paniagua et al., 2018). At that latitude, the core of the current is observed above the 1000 m isobath (Vivier and Provost, 1999b; Spadone and Provost, 2009) and its flow might suffer large deflections for several months caused by the southward excursions of the Brazil Current (Paniagua et al., 2018). Indeed, the encounter between the MC and the southward flowing Brazil Current makes difficult to quantify the MC variability at 40-41°S (Ferrari et al., 2017).

Further south, the first direct observations of surface currents over the shelf break were registered at 45°S by hull-mounted downward-looking ADCP observations in late December 1992 (Saunders and King, 1995). The ADCP meridional velocity component in the 30-390 m depth interval presents an energetic northward flow spanning nearly 150 km (Saunders and King, 1995). Valla and Piola (2015) analyzed 52-days of direct current observations in 2005 from a downward-looking ADCP moored close to the upper portion of the shelf break at 43.8°S and showed that the mean flow is strongly steered by the bottom topography. The combined analysis of surface drifters, satellite-derived geostrophic velocity and the ADCP data from Saunders and King (1995) showed that the MC flow at 45°S is mainly concentrated in two narrow jets located just onshore of the 200 m and over the 1400 m isobaths (Piola et al., 2013). Surface velocities within the jets exceed 0.5 m s⁻¹. These jets extend more than 900 km from 47.5°S to 39°S along the Patagonian shelf break (Piola et al., 2013). Moreover, recent analyses of repeated hull-mount ADCP observations indicate that these two high-velocity jets are observed along the entire MC path from the northern Drake Passage to the Brazil/Malvinas Confluence (Frey et al., submitted). Numerical simulations partially agree with this observation: Fetter and Matano (2008) and Combes and Matano (2014) reported the presence of two jets extending from 55°S and merge at approximately 45°S.

1
2
3
4
5
6
7
8
9
10
11
12
13
14
15
16
17
18
19
20
21
22
23
24
25
26
27
28
29
30
31
32
33
34
35
36
37
38
39
40
41
42
43
44
45
46
47
48
49
50
51
52
53
54
55
56
57
58
59
60
61
62
63
64
65

85 The surface thermal structure between 39° and 44°S and along the western limb of the MC is
86 characterized by multiple fronts (Franco et al., 2008). Piola et al. (2013) pointed out the association
87 between the time-averaged SST fronts and high-velocity jets of the MC. They showed that the
88 location of the two across-shelf SST gradient minima, described for the first time by Franco et al.
89 (2008), coincide with the two maxima satellite-derived meridional velocities that they found at
90 45°S. These latter findings motivate a recent study that confirm, using deterministic and
91 probabilistic tools from nonlinear dynamics, the expectation that the MC behaves as a barrier for
92 cross-stream transport (Beron-Vera et al., 2020). Consequently, south of 38°S, the MC promotes
93 low connectivity between shelf waters and open-ocean waters off the shelf (Beron-Vera et al.,
94 2020).

95
96 Furthermore, high chlorophyll-a concentrations observed during the austral spring and summer
97 over the shelf break (Romero et al., 2006; Saraceno et al., 2005) suggest that the nutrient-rich
98 subantarctic waters advected by the MC contributes to the large phytoplankton biomass observed
99 along the shelf break (Acha et al., 2004; Romero et al., 2006). Indeed, the high productivity found
100 in the shelf break front (Garcia et al., 2008; Lutz et al., 2010) is the main ecological feature that
101 supports the production of tangible (fisheries) and intangible (recreation, regulation of atmospheric
102 gases) marine ecosystems services (Martinetto et al., 2020). In particular, physical process along
103 the shelf break sustain one of the most important fisheries of scallops in the southern hemisphere
104 (Franco et al., 2017).

105
106 Several mechanisms have been proposed to explain the physical mechanism that sustain the
107 primary productivity over a continental slope: enhanced mixing through tidal interaction with the
108 continental slope (Rattray, 1960), the interleaving of water masses at the shelf break front
109 (Fournier et al., 1979), the interaction between shelf-edge wave propagating northward along the
110 slope and bottom topography (Dickson et al., 1980; Acha et al., 2004; Saraceno et al., 2005), the
111 interaction of internal waves at the shelf break and wind-induced mixing (Maze et al., 1986), small-
112 scale eddies propagating along the edge of the Malvinas Current (Podestá et al., 1990), horizontal
113 divergence of the surface velocity field generated by the effect of bottom friction on the MC along
114 the Patagonian shelf break (Matano and Palma, 2008; Combes and Matano, 2014) and wind-
115 induced upwelling (Carranza et al., 2017). Yet, to the best of our knowledge, direct observations

1
2
3
4 116 that may help elucidate which mechanisms contribute most to sustain the primary productivity
5
6 117 observed, have not been reported.
7

8 118
9
10 119 The main objective of this work is to characterize the MC velocities through the analysis of the in
11
12 120 situ measurements collected at 44.7°S between December 2015 and June 2017. Improving the
13
14 121 knowledge of MC dynamics is the first step to better understand the process that sustain the rich
15
16 122 Patagonian shelf break ecosystem in future studies. In situ data analyzed on this work were
17
18 123 obtained in the framework of the French-Argentine CASSIS project
19
20 124 (www.cima.fcen.uba.ar/malvinascurrent). During 2015-2017, an array of nine mooring was
21
22 125 deployed over a zonal section at 44.7°S across the continental shelf and shelf break (Figure 1a). In
23
24 126 this study we focus on the analyses of the shelf break moorings. In section 2, we describe the data
25
26 127 and methods used. In Section 3 we first present the results obtained through a statistical analysis
27
28 128 of all in situ currents. We then focus on the possible mechanisms that cause the observed variability
29
30 129 by combining the in situ velocity observations with satellite altimetry data. Sections 4 presents a
31
32 130 discussion of the results and section 5 summarizes the conclusions.
33

34 131 35 132 **2. Data and Methods**

36 133 **2.1. In situ Data**

37 134 Nine current meter moorings were deployed in a zonal section, spanning the wide continental shelf
38
39 135 and slope of the western margin of the Argentine Basin at 44.7°S (Figure 1). Four moorings were
40
41 136 deployed in the continental shelf and five over the shelf break and upper continental slope,
42
43 137 perpendicularrly to the main direction of the isobaths (Figure 1a), from 1 December 2015 to 9 June
44
45 138 2017. In this study we examined the current meter data obtained across the continental slope
46
47 139 (Figure 1b; Table 1). These moorings were deployed between the 200 and 2600 m isobaths (Figure
48
49 140 1; Table 1). From shallow to deep waters, the array consisted of a surface oceanographic buoy,
50
51 141 one upward looking Acoustic Doppler Current Profiler (ADCP) and three tall-moorings referred
52
53 142 to as M1, M2 and M3 (Figure 1). The oceanographic buoy was moored at 200 m depth and was
54
55 143 equipped with a hull-mounted downward-looking Nortek Continental 190 kHz ADCP with an
56
57 144 accuracy of 1% of the measured value and a resolution of 0.1 cm s⁻¹. The buoy was detached form
58
59 145 its mooring 22 days after deployment. The upward looking ADCP was deployed at 1000 m depth
60
61 146 but could not be recovered. The three tall-moorings were deployed over the 1320 m, 1945 m and
62
63
64
65

1
2
3
4
5
6
7
8
9
10
11
12
13
14
15
16
17
18
19
20
21
22
23
24
25
26
27
28
29
30
31
32
33
34
35
36
37
38
39
40
41
42
43
44
45
46
47
48
49
50
51
52
53
54
55
56
57
58
59
60
61
62
63
64
65

147 2608 m isobaths and comprised eleven Nortek Aquadopp current meters deployed at different
148 depth (Figure 2). The measurement accuracy of Aquadopp current meters is 1% of the measured
149 value $\pm 0.5 \text{ cm s}^{-1}$. M1 and M2 were deployed on November 26, 2015 and the oceanographic buoy
150 and M3 between 13 and 16 May 2016. Hereinafter, instruments installed in the tall-moorings are
151 labelled M_{ij} where i represents the mooring number and j stands for the position within the
152 mooring from the upper to the deepest instrument (Figure 2). Current meters moored on the tall-
153 moorings M1 and M2 recorded data every half hour. Current meters on M3 recorded hourly data.
154 Different sampling frequencies were adopted to optimize the number of samples, battery
155 consumption, and memory capacity of each instrument as well as the aimed duration of the
156 experiment.

157
158 The three tall-moorings were recovered between 8 and 10 June 2017. All current meters on M1
159 produced 528 to 554 days of high-quality data. Current meters on M3 recorded data for 390 days.
160 Occasionally, the tall-moorings suffered large vertical displacements of up to 120 m that lasted as
161 much as a few days. These events coincide with the largest MC intensities recorded. One month
162 after deployment, M2 was accidentally lifted by a fishing vessel, dragged and released about 5 km
163 east from the original location. As a result, the depth of the final position of M2 was 600 m deeper.
164 Hereinafter we denote $M2_a$ the first 1 month-period of measurements (December 2015) and $M2_b$
165 the second and longest observation period (January 6, 2016 to June 9, 2017) (Figure 2). Table 2
166 summarizes data availability and basic statistics measured by the current meters. All data used in
167 this work are available in Saraceno et al. (2020).

168

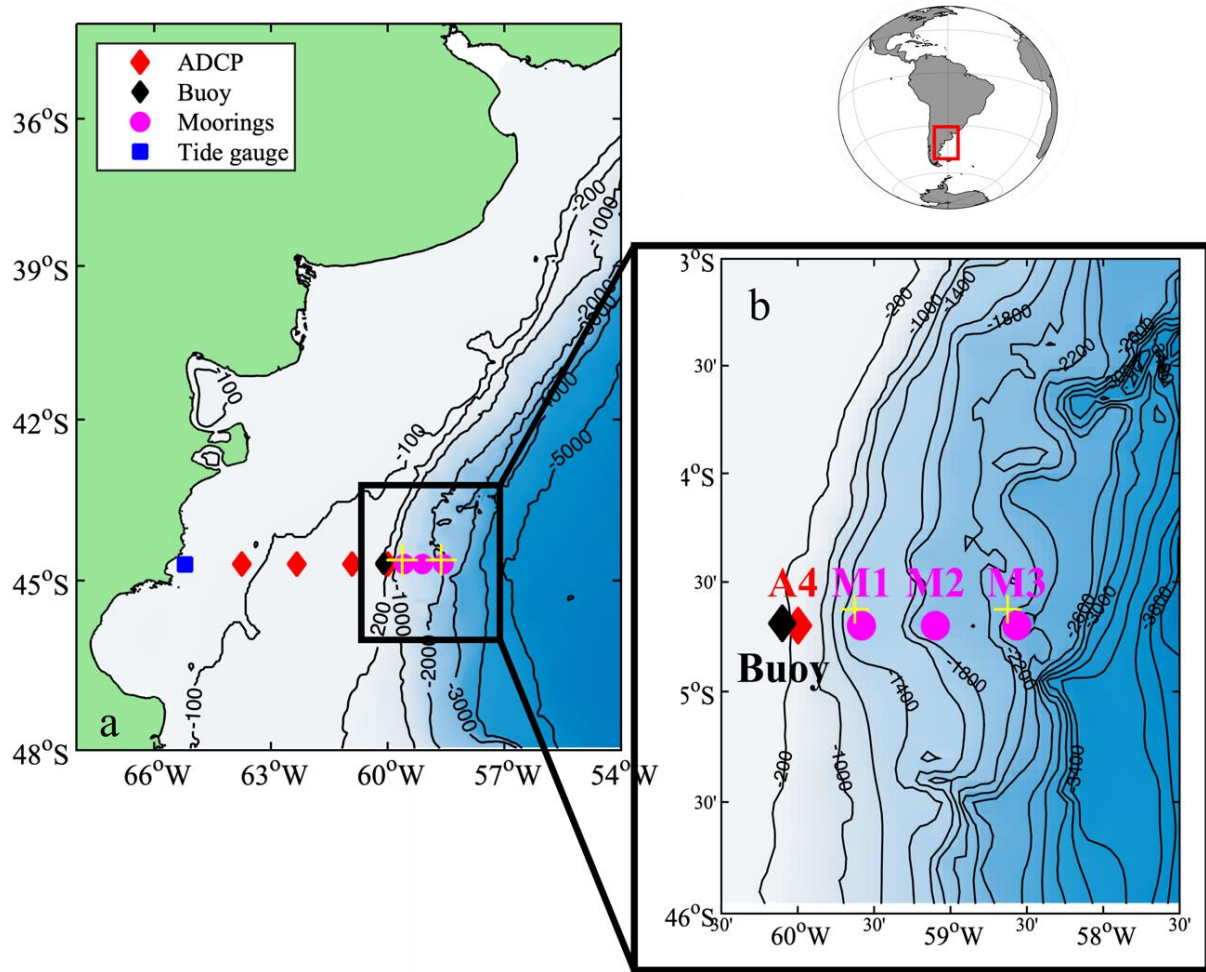


Figure 1. (a) Study region, moorings position and bathymetry. Color symbols represent the location of the moorings of the CASSIS project. The 100, 200, 1000, 2000 and 4000 m isobaths are indicated in black (GEBCO, (IOC, 2003)). (b) Enlarged map showing the location of the mooring array deployed in the shelf break from December 2015 to June 2017. The oceanographic buoy, the upward-looking ADCPs and the three tall-moorings are indicated with black and red diamonds and magenta circles respectively. The yellow crosses indicate the location from which the altimetry data were extracted to compare in-situ and satellite altimetry data.

1
2
3
4 178
5
6 179
7
8 180
9
10 181
11
12
13
14
15
16
17
18
19
20
21
22
23
24
25
26
27
28
29
30
31
32
33
34
35
36
37
38
39
40
41
42
43
44
45
46
47
48
49
50
51
52
53
54
55
56
57
58
59
60
61
62
63
64
65

1
2
3
4
5
6
7
8
9
10
11
12
13
14
15
16
17
18
19
20
21
22
23
24
25
26
27
28
29
30
31
32
33
34
35
36
37
38
39
40
41
42
43
44
45
46
47
48
49
50
51
52
53
54
55
56
57
58
59
60
61
62
63
64
65

182

183

184 **2.2. Satellite Data**

185 To examine the regional mesoscale field we used maps of absolute dynamic topography (MADT)
186 derived from satellite altimetry and associated geostrophic velocities. Both altimeter products were
187 downloaded from the Copernicus Marine Environment Monitoring Service
188 (CMEMS, <http://marine.copernicus.eu>) site for the period 1993-2017. MADT and geostrophic
189 velocities maps have a daily frequency and a horizontal resolution of 0.25x0.25 degree in a
190 cartesian regular grid. Geostrophic velocity derived from satellite altimetry can be derived from
191 gridded data constructed from multiple missions or from along-track mono-mission data. Gridded
192 data compare better with in situ data than along-track data (Ferrari et al., 2012; Ferrari et al 2017).
193 The agreement between in situ and satellite-derived velocities increases when a 20-day low-pass
194 filter is applied to the in situ data (Ferrari et al., 2017).

195

196 **2.3. Methods**

197 All meridional (v) and zonal (u) velocity components were low-pass filtered with a cut-off period
198 of 48 hours to remove tidal and inertial variability. Statistical parameters including mean and
199 standard deviation of all low-pass filtered variables are given in Table 2 and Table 3. Spectra,
200 confidence limits (CL) and significant peaks of the time series are calculated using the singular
201 spectrum analysis multitaper method toolkit (Ghil et al., 2002). Two data tapers are used, and
202 significant peaks have been estimated with the hypothesis of a harmonic process drawn back in a
203 background red noise.

204

205 **3 Results**

206 **3.1. Variability of the MC from in situ data**

207 *3.1.1. Velocity time series*

208 All raw and 48h-low-pass filtered meridional and zonal velocities time series are displayed in the
209 supplementary material (Figures S1-S9). A description of the low-pass filtered meridional and
210 zonal velocities time series follows.

211

212 Oceanographic buoy

1
2
3
4 213 The meridional (along-isobath) velocity observed at the oceanographic buoy was always positive
5
6 214 and reached maximum values of 68 cm s^{-1} at 20 m depth. The zonal velocity values at 20 m depth
7
8 215 ranged between -13 cm s^{-1} (onshore) and 10 cm s^{-1} (Figure S1) suggesting significant cross-shelf
9
10 216 break exchanges, though mean zonal (cross-shelf break) velocities are close to zero in the entire
11
12 217 water column (see supporting information in Figure S1 and Table 3). Similar characteristics were
13
14 218 reported by Valla and Piola (2015) based on a 52-day current meter time series at approximately
15 219 the same location.
16

17 220

18

19 221 M1

20 222 The meridional velocity component observed at M1 was positive most of the time at all depths
21
22 223 (Figure 3a and supporting information Figures S2a, S3a and S4a). No meridional reversals were
23
24 224 observed in the shallowest instrument moored at 300 m depth (M11) and only one flow reversal
25
26 225 event was recorded at 760 m depth (M12) in July 2016, and on six occasions at 1042 m depth
27
28 226 (M13). The flow reversals lasted between one and seven days. As in the shelf edge, the meridional
29
30 227 velocity was much larger than the zonal velocity, reaching maximum values of 61.4 cm s^{-1} at M11
31
32 228 (300 m, Figures 3a and supporting information Figure S2a). In addition, all records at M1 present
33
34 229 large oscillations (up to 50 cm s^{-1}) in the meridional velocity at all depths (Figure 3a). As will be
35
36 230 shown later, these oscillations appear to be generated by mesoscale structures that interact with the
37
38 231 the bathymetry further south. On the other hand, the zonal components of the currents at M1 show
39
40 232 values ranging between -22 cm s^{-1} and 24 cm s^{-1} with mean values close to zero in the entire water
41
42 233 column (Figure 3c, supporting information Figures S2b, S3b and S4b and Table 2).
43

44 234

45 235 M2

46 236 Meridional velocities at M2_a were always northward (positive) down to 1315 m depth. Only two
47
48 237 flow reversals were recorded at 1720 m depth, the deepest current meter deployed at M2_a (Figures
49
50 238 S5a, S6a and S7a). The zonal velocity values at M2_a fluctuated between -17 cm s^{-1} and 26 cm s^{-1}
51
52 239 and the mean zonal velocity was close to zero, as observed at M1 (Figure S5b, S6b and S7b; Table
53
54 240 2).

55 241

57 242 After M2 was displaced eastward, the whole mooring dropped 600 m, so all observations were
58
59 243 recorded between 1560 and 2270 m depth. At M2_b we observed a different behavior compared to
60
61
62
63
64
65

1
2
3
4
5
6
7
8
9
10
11
12
13
14
15
16
17
18
19
20
21
22
23
24
25
26
27
28
29
30
31
32
33
34
35
36
37
38
39
40
41
42
43
44
45
46
47
48
49
50
51
52
53
54
55
56
57
58
59
60
61
62
63
64
65

244 M2_a. The meridional velocity component observed at M22_b (1560 m) and M23_b (1865 m) were
245 positive most of the time, while at M24_b (2270 m), the meridional velocity fluctuated around zero
246 as well as the zonal velocities observed at all depths at this location (Figures S5a, A6a and S7a).
247 An interesting observation is that the amplitude of the oscillations at M22_b, M23_b and M24_b of the
248 zonal currents increases with depth (Figure S5b, S6b and S7b).

249

250 M3

251 At M3, the easternmost tall-mooring, current velocity was measured at four levels ranging from
252 500 to 2100 m depth (Figure 2). As observed at M1 and M2_a, the meridional velocities were
253 positive almost of the time except in a few occasions when current reversals were observed. During
254 the time period analyzed here, the instruments recorded a minimum of one to a maximum of
255 fourteen meridional flow reversals and the number of reversals increased downward (Figure 3e
256 and supporting information Figures S8a, S8c, S9a and S9c). Furthermore, large oscillations were
257 present in the meridional velocity at all depths as observed at M1. The average zonal velocity of
258 the four current meters is not significantly different from zero (Table 2). The amplitude of the
259 oscillations of the zonal velocities recorded at M3 are much larger than those observed at M1
260 (Figure 3g and supporting information Figures S8b, S8d, S9b and S9d).

261

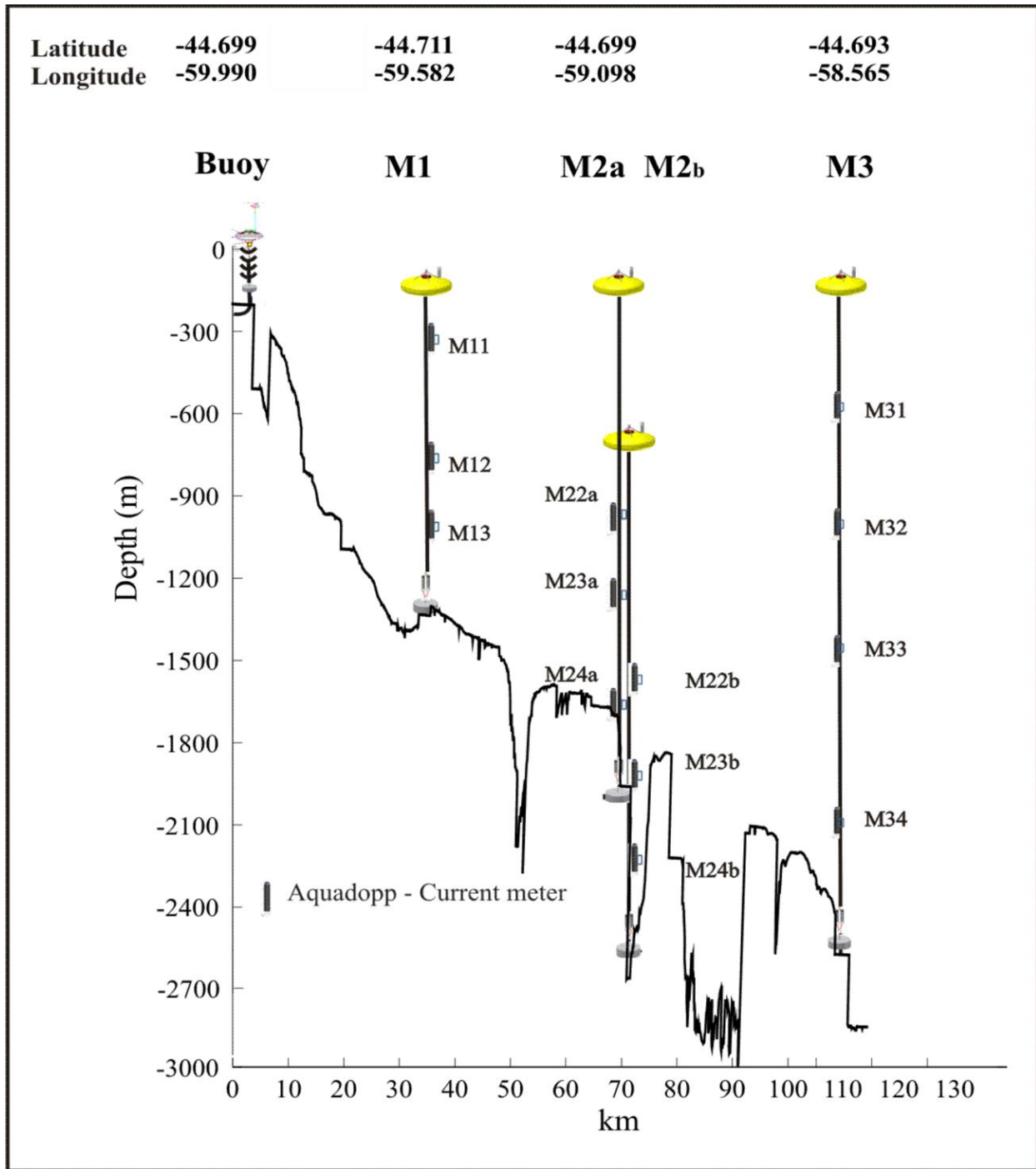


Figure 2. Location and vertical distribution of the current meters deployed along 44.7°S between December 2015 and June 2017. The oceanographic buoy was the only mooring with a surface buoy that transmitted data on real-time. It was deployed at 200 m depth. The bathymetry displayed was reconstructed with echo-sounder data obtained during the deployment cruises.

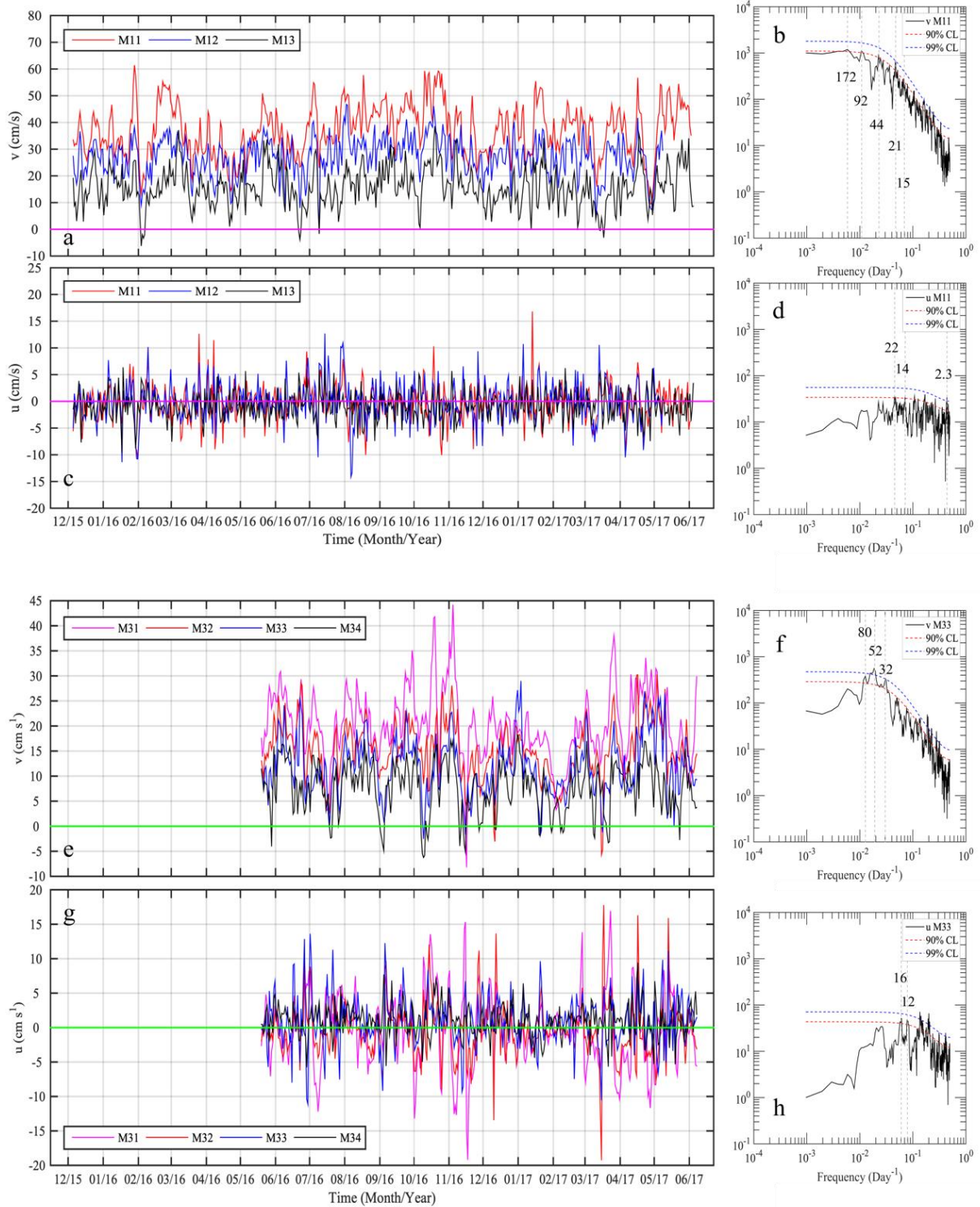


Figure 3. In situ time series of meridional and zonal velocities observed at M1 (a, c) and M3 (e, g). Color lines correspond to 48 h low-pass filtered daily data. Horizontal magenta and green lines

1
2
3
4 272 indicate the zero value. Spectra ((cm/s)²/cpd) of meridional and zonal currents at (b, d) 300 m
5
6 273 (M11) and at (f, h) 1486 m (M33). The red and blue dashed lines in all the right panels, indicate
7
8 274 90% and 95% confidence levels (CL), respectively. Also, the black vertical dashed lines and the
9
10 275 associated numbers indicate significant periodicities in days. See Figure 2 for spatial location of
11
12 276 the moorings.

13 277

14
15 278

17 279 3.1.2. Mean velocity and velocity variance ellipses

18
19 280 Time and depth average current velocities are 46.6, 27, 16, 5.1, and 13.8 cm s⁻¹ at the
20
21 281 oceanographic buoy, M1, M2_a, M2_b, and M3, respectively. The relatively low mean velocity
22
23 282 observed at M2_b is due to the fact that all observations are deeper than 1500 m. As the direction of
24
25 283 the mean flow at M1, M2_a and M3 is northward, we conclude that the mean flow at this latitude is
26
27 284 strongly constrained by the local bathymetry (Figure 4). At all locations the mean velocities
28
29 285 decrease with depth (Figure 4; Tables 2 and 3), suggesting an equivalent-barotropic structure as
30
31 286 previously reported based on observations at 41°S (e.g. Vivier and Provost, 1999b). Through the
32
33 287 entire water column, the time-averaged velocities observed at M1 are higher in comparison with
34
35 288 the time-averaged velocities observed at the easternmost mooring: the mean values range between
36
37 289 37.3 cm s⁻¹ at 300 m (M11) and 16.1 cm s⁻¹ at 1042 m depth (M13) (Figure 4; Table 2). The large
38
39 290 mean values observed at M1 suggest that the MC is stronger at this longitude, in good agreement
40
41 291 with observations made from previous snap-shot observations at 45°S (Saunders and King, 1995;
42
43 292 Piola et al., 2013, Frey et al., 2020). The direction of the major axes of the variance ellipses is
44
45 293 northward, indicating that the largest fluctuations occur in the same direction of the mean flow at
46
47 294 all moorings and depths, except close to the bottom at M2_a (1720 m) and at all depths at M2_b
48
49 295 (Figure 4). The distinct observations collected at M2_b will be described separately below. The
50
51 296 variability of the zonal component is higher at M3 compared with M1 (Figure 4) because M3 is
52
53 297 more exposed to the intense mesoscale activity present in the open ocean (Figure 1). This
54
55 298 observation is in agreement with previous reports of the variability of the zonal component of the
56
57 299 MC at 41°S (e.g. Paniagua et al., 2018).

58 300

59 301 The direction of the mean flow and the variance ellipses at M2_b (Figure 4) are quite different from
60
61 302 those observed at M1 and M3. The mean flow direction in the upper two instruments (M2_{2b} and
62
63
64
65

1
2
3
4
5
6
7
8
9
10
11
12
13
14
15
16
17
18
19
20
21
22
23
24
25
26
27
28
29
30
31
32
33
34
35
36
37
38
39
40
41
42
43
44
45
46
47
48
49
50
51
52
53
54
55
56
57
58
59
60
61
62
63
64
65

M23_b located at 1560 m and 1865 m depth) is towards the northeast, with means exceeding the standard deviations. The deepest instrument (M24_b at 2270 m depth) shows a nearly zero velocity mean and a velocity variance ellipse oriented nearly perpendicular to the direction of the mean MC flow (Figure 4). The bathymetry was recorded by a Kongsberg EA600 12/600 kHz single beam hydrographic echo sounder on the R/V Puerto Deseado during the deployment cruise over the moorings (displayed in Figures 2 and 4). The mean velocity vectors and variance ellipses observed at M23_b (1865 m) and M24_b (2270 m) (Figure 4) suggests that these observations were collected within a a hole or a submarine canyon with a southwest-northeast orientation, i.e. parallel to the mean axis of variance the flow at M24_b. The latter results clearly suggests that the flow at M24_b is strongly controlled by the local bathymetry. Submarine canyons are quite common in the region (Lastras et al., 2011), despite their location is not reported in the majority of seafloor maps. While the analysis of the flow into the submarine canyon is certainly very interesting, it is out of the scope of this work and will not be covered within this article.

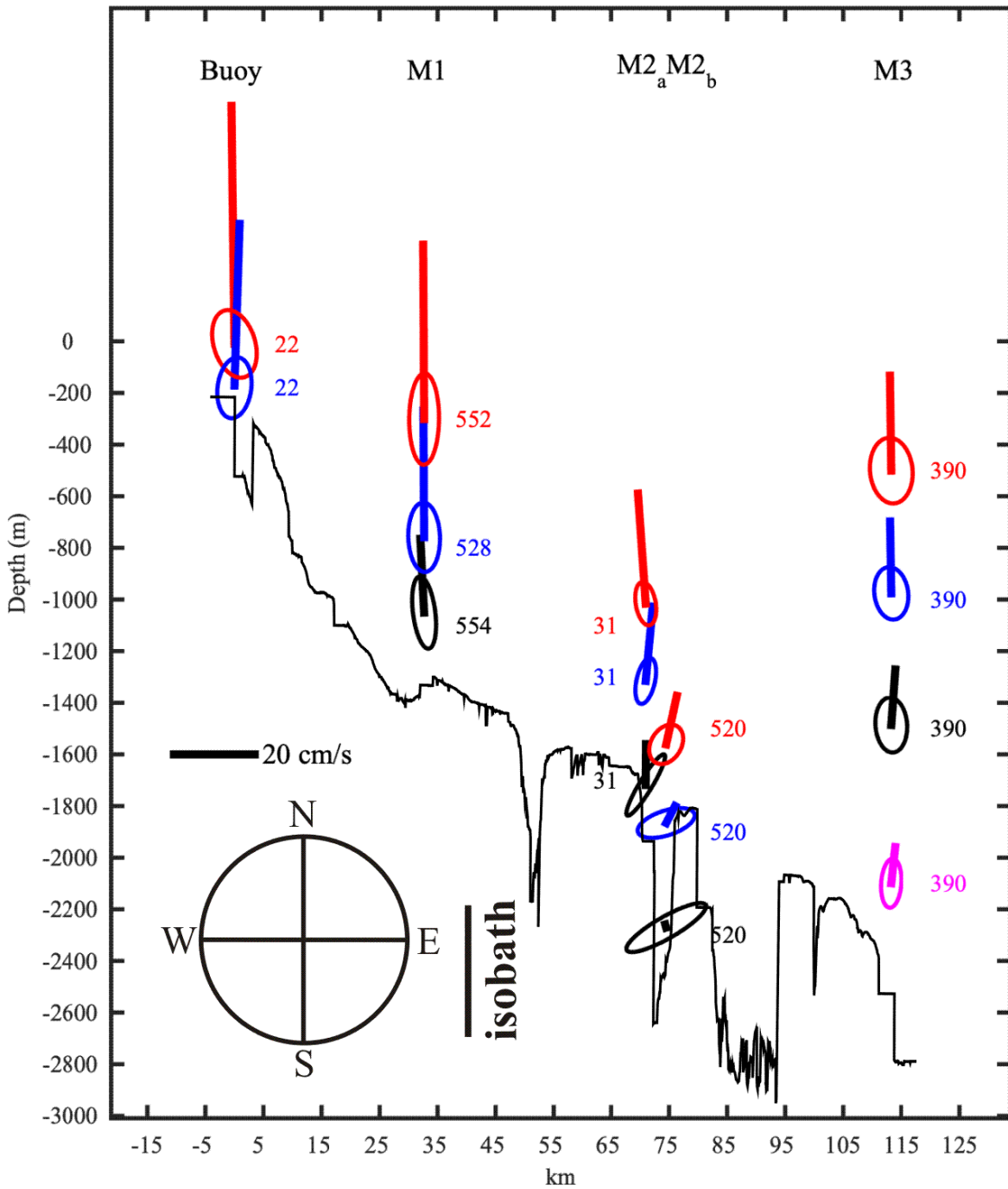


Figure 4. Mean flow and variance ellipses of the time series obtained by the current meters. The number of days that each instrument measured are indicated. The average orientation of the isobaths at 44.7°S is indicated by the thick line at the bottom. The black line corresponds to the topography along the section where the moorings were deployed. The X axis is the distance along the section in km, the origin being the buoy location.

1
2
3
4
5
6
7
8
9
10
11
12
13
14
15
16
17
18
19
20
21
22
23
24
25
26
27
28
29
30
31
32
33
34
35
36
37
38
39
40
41
42
43
44
45
46
47
48
49
50
51
52
53
54
55
56
57
58
59
60
61
62
63
64
65

322

323

3.1.3. Spectral and vertical coherence analysis of the velocity time series measured on the MC

The meridional and zonal velocity time series observed at M1 and M3 show a vertically coherent flow (Figures 3a, 3c, 3e and 3g). To determine the scales that dominate the time variability of the flow we estimate the spectra of the meridional and zonal components of the current velocity registered at M1 and M3. The spectral analysis of all the meridional components measured at M1 and M3 show significant periodicities around 85, 40, 20 and 15 days (Figure 3). In addition, the spectral estimates of the zonal component at M1 and M3 reveals significant peaks in a broad band of periodicities between 25 and 2 days (Figure 3). The spectra of the zonal velocity at M34 (2100 m) denoted significant periodicities centered at 55 days (not shown).

The vertical coherence between the meridional and the zonal velocity components at M1 shows, in most cases, that the two components are coherent at 52, 25, 18 and 13 days (Figures S10a and S10b). The coherence analysis carried out between the meridional and zonal velocities at M31 (500 m), M32 (976 m) and M33 (1486 m) denoted a significant vertical coherence at 38, 19, 13 and 8 days (Figures S10c and S10d). No significant coherence was observed between M34 and the shallower observations at that location. This suggests that the processes that induce the velocity variations at 2100 m depth, near the seabed, are uncoupled from those that modulate the velocity variability at shallower levels.

3.1.4. Principal modes of variability of the MC velocities

To further quantify the variability of the vertical structure of the MC, we computed empirical orthogonal functions (EOFs) of the time series collected at M1 and M2. The spatial patterns of the three leading modes and the time series associated with moorings M1 and M3 are displayed in Figure 5.

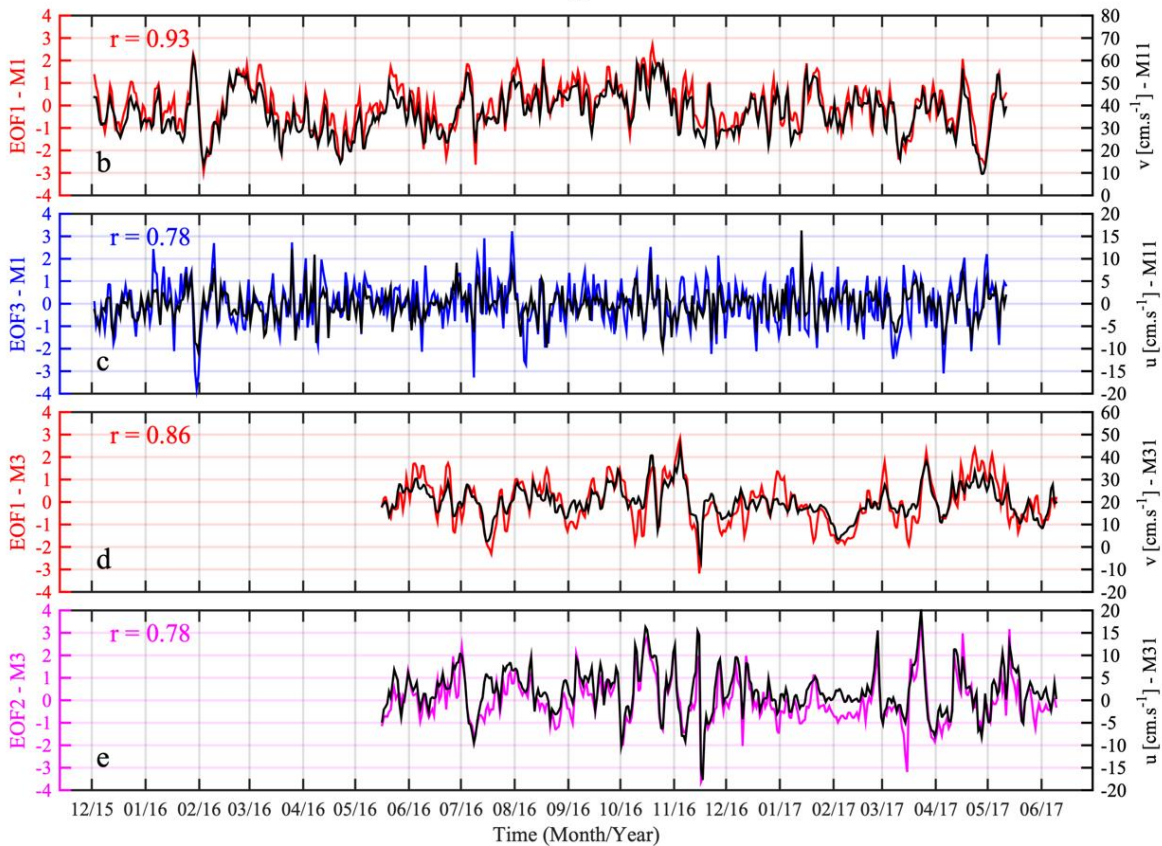
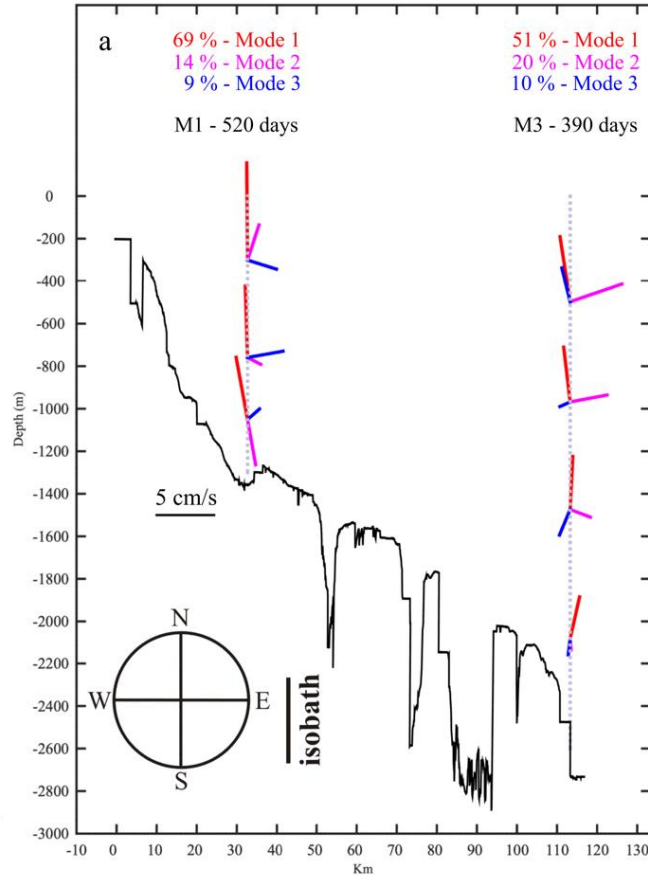
The first leading EOF (EOF1) of M1 and M3 explains 69% and 51% of the total variance, respectively (Figure 5a). The spatial patterns of EOF1 at M1 and at M3 (Figure 5a) and the high correlations between the time series of respective EOF1 and the meridional velocity at M11 (0.93, 95% CL) and M31 (0.86, 95% CL) (Figures 5b and 5d) clearly characterize this mode as an along-isobath mode of velocity fluctuations. The spatial pattern of EOF1 at M1 is surface-intensified and

1
2
3
4
5
6
7
8
9
10
11
12
13
14
15
16
17
18
19
20
21
22
23
24
25
26
27
28
29
30
31
32
33
34
35
36
37
38
39
40
41
42
43
44
45
46
47
48
49
50
51
52
53
54
55
56
57
58
59
60
61
62
63
64
65

353 has a downward counter-clockwise rotation with depth while the spatial mode of EOF1 at M3
354 shows similar intensities in the vertical and a downward clockwise rotation (Figure 5a).

355
356 EOF3 of M1 and EOF2 of M3 explain 9% and 20% of the total variance, respectively (Figure 5a)
357 and represent variations in the across-isobath velocity at M1 and M3. This is confirmed by the
358 high correlations (0.78, 95% CL) between the associated time series of these modes and the zonal
359 velocity component at the shallowest observed level at each location (Figure 5 c and e).

1
2
3
4
5
6
7
8
9
10
11
12
13
14
15
16
17
18
19
20
21
22
23
24
25
26
27
28
29
30
31
32
33
34
35
36
37
38
39
40
41
42
43
44
45
46
47
48
49
50
51
52
53
54
55
56
57
58
59
60
61
62
63
64
65



1
2
3
4
5
6
7
8
9
10
11
12
13
14
15
16
17
18
19
20
21
22
23
24
25
26
27
28
29
30
31
32
33
34
35
36
37
38
39
40
41
42
43
44
45
46
47
48
49
50
51
52
53
54
55
56
57
58
59
60
61
62
63
64
65

Figure 5. (a) Spatial pattern of the empirical orthogonal functions (EOFs) of the velocity field of M1 and M3 tall-moorings; the percentage of total variance explained by mode 1, 2 and 3 of each EOF is denoted in red, magenta and blue, respectively. EOFs are computed separately for each mooring. The average orientation of the isobaths is indicated by the thick line at the bottom. Vertical scale in meters; horizontal scale in kilometres. (b) Time series of EOF1 at M1 (red) and meridional velocity (cm s^{-1}) at M11 (black). (c) Time series of EOF3 at M1 (blue) and zonal velocity (cm s^{-1}) at M11 (black). (d) Time series of EOF1 at M3 (red) and meridional velocity (cm s^{-1}) at M31 (black). (e) Time series of EOF2 at M3 (magenta) and zonal velocity (cm s^{-1}) at M31 (black). In the four bottom panels, the correlation between time series is indicated in the top left corner.

3.1.5. Spectral analysis of the EOFs time series

The spectra of EOF1 at M1 and M3, that characterize the along-isobath (meridional) velocity variations, show significant periodicities (Figure S11, a-b) similar to those described in section 3.1.4 in the spectral analysis performed for each meridional velocity time series measured at M1 and at M3, respectively (Figures 3b and 3f). In addition, EOF3 which characterizes the zonal velocity variability at M1 showed significant peaks in the same frequency band (Figure S11c) as all the zonal velocity time series at M1 (Figure 3d). On the other hand, the spectra of EOF2 at M3 displays a significant periodicity centered at 25 days (Figure S11d). The 25-day peak was only significant in the spectral estimates of the zonal velocity component observed at M31 (300 m depth) and M32 (1070 m depth) (not shown). The wavelet power spectra of the EOFs time series indicates that those periodicities occur seldomly (Figures S12 and S13). This suggests that several processes force the observed oscillations and that those processes are not periodic in time. In the following section we show that the propagation of SLA are a likely contributor to this velocity variability pattern.

3.2. On the origin of the MC variability at 44.7°S

In the following section we first compare the 20-day low pass in situ velocities with the geostrophic velocities computed from satellite gridded altimetry data closest to M1 and M3 locations. We then

1
2
3
4
5
6
7
8
9
10
11
12
13
14
15
16
17
18
19
20
21
22
23
24
25
26
27
28
29
30
31
32
33
34
35
36
37
38
39
40
41
42
43
44
45
46
47
48
49
50
51
52
53
54
55
56
57
58
59
60
61
62
63
64
65

391 use satellite altimetry data to unveil the origin of the oscillations observed in the in situ velocity
392 described in Section 3.1.

393 394 3.2.1. Comparison between in situ and satellite altimetry velocities

395 The 20-day low-pass filtered meridional and zonal velocities at 300 m depth at M1 are significantly
396 correlated with the meridional and zonal velocities derived from gridded satellite altimetry data
397 closest to the mooring location (0.74 and 0.55, respectively, Figures 6c and 7c). At M31 (500 m
398 depth) the correlations of the meridional and zonal velocities with the altimetry derived velocities
399 are higher: 0.80 and 0.85, respectively (Figures 6a and 7a). Therefore, in agreement with previous
400 studies (Ferrari et al., 2017) satellite altimetry appears to be a good proxy to monitor currents at
401 periods longer than 20 days. However, some of the largest oscillations present in the low-pass
402 filtered in situ velocities (e.g. oscillations of up to 50 cm s⁻¹ in less than a week in the meridional
403 velocities at M11 and at M31; grey line in Figures 6a and 6c) are not captured by altimetry data.

404
405 At M1 (M3), the mean meridional velocity obtained from altimetry between December 2015-June
406 2017 (May 2016-June 2017) is 7 (6) cm s⁻¹ larger than the mean value of the meridional velocity
407 component observed at the shallowest current meter moored at M11 (M31) around 300 m (500 m)
408 depth (Tables 3 and 4). This result is expected since the MC flow has a barotropic-equivalent
409 structure and, therefore, the magnitude of the velocity decreases with depth. On the other hand, the
410 satellite-derived current velocities do not represent the most superficial currents of the ocean.
411 Indeed, at the buoy, the comparison between satellite altimetry and in situ velocities recorded by
412 the downward-looking ADCP at 10 m intervals in the whole water column, shows that the best
413 match occurs at 120 m depth (Table 3).

414 415 3.2.2. Variability of the MC in time and space

416 Given the significant correlation between satellite altimetry and in situ velocities, to better
417 understand the variability observed at the mooring locations we used the MADT and derived
418 geostrophic velocities to examine the two-dimensional surface flow field. In spite of the proximity
419 between M1 and M3 (80 km), the correlation between the satellite-derived meridional velocities
420 is non-significant ($r = -0.05$ and $p\text{-value} = 0.26$). Furthermore, the mean satellite-derived
421 meridional component at M1 location is almost twice as large as that observed at M3 (Figure 6b;

1
2
3
4 422 Table 4). On the other hand, a significant, though low correlation is found between satellite-derived
5
6 423 zonal velocities at M1 and M3 ($r = 0.33$ and $p\text{-value} = 1 \times 10^{-15}$). In this case, the mean zonal
7
8 424 velocity at M1 is four times larger than the mean value observed at M3 (Figure 7b; Table 4).
9

10 425
11 426 A longitude versus time diagram of satellite-derived meridional velocities across the mooring
12
13 427 section during the study period (Figure 6b) suggests an explanation for the different variability
14
15 428 patterns observed at M1 and M3. The temporal mean of the meridional velocity derived from
16
17 429 satellite altimetry along the section between 62°W and 57°W suggest that the core of the MC ($>$
18
19 430 40 cm s^{-1}) lies very close ($\sim 20 \text{ km}$) to M1 (Figure 6b, left panel). In mid-April 2016, a sharp
20
21 431 decrease in meridional velocities (from 45 cm s^{-1} to less than 30 cm s^{-1} based on the altimetry data)
22
23 432 was observed throughout the entire section. On the other hand, from August to November 2016,
24
25 433 the MC increased its intensity reaching a maximum of 62.5 cm s^{-1} in August. In late April 2017,
26
27 434 the core of the MC moved closer to M3 (Figure 6b, right panel). This last event generated a large
28
29 435 increase (decrease) in the meridional velocity over M3 (M1) (Figures 6a and 6c). In the following
30
31 436 section we will discuss the possible origin of the variability observed in the meridional velocities
32
33 437 at M1 and M3.
34

35 438
36 439 We also analyzed the longitude versus time diagram of the satellite-derived zonal velocities along
37
38 440 the section at 44.7°S and between 62 and 57°W during the study period (Figure 7b). The time mean
39
40 441 zonal velocity is highest ($\sim 4.5 \text{ cm s}^{-1}$) very close to the shelf break, suggesting a weak net offshore
41
42 442 flow. This is the only portion of the section where the time mean is significantly different from
43
44 443 zero. In addition, the cross-shore velocity standard deviation increases from the edge of the shelf
45
46 444 break to the open ocean (Figure 7b, left panel). Between M1 and M3 the zonal velocities are low
47
48 445 and are negative on several occasions (Figure 7b, right panel).
49
50 446
51 447
52 448
53 449
54
55
56
57
58
59
60
61
62
63
64
65

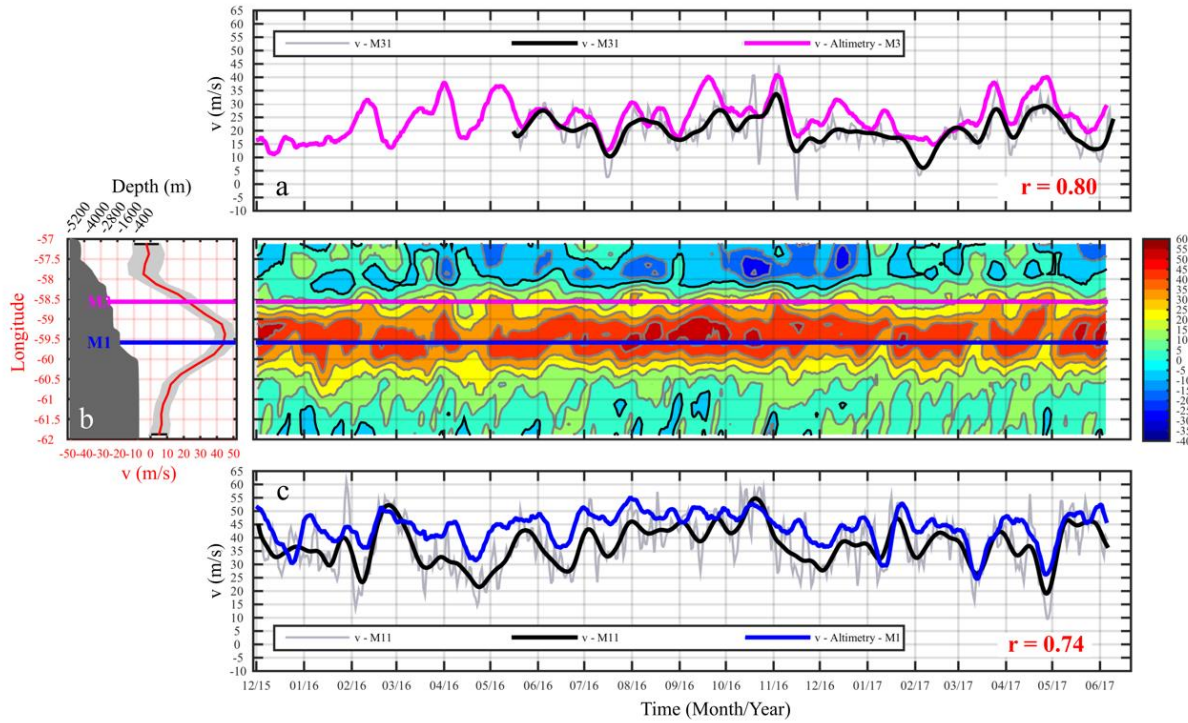


Figure 6. (a) In situ time series of the 2 and 20 days low-pass filtered daily resampled meridional velocity component at M31 are indicated with grey and black lines, respectively. The magenta line shows the time series of the meridional component of the surface velocity derived from satellite altimetry near M3. Correlation between the 20-day low pass filtered in situ time series and the altimeter time series is indicated in the bottom right corner. (b) Right panel: Longitude vs time plot of the meridional component of the current derived from satellite altimetry along 44.7°S and between 62 and 57°W. The blue (magenta) line represent the longitude of M1 (M3). Left panel: mean (red) and standard deviations (grey shading) of the meridional velocity derived from the altimeter. The topography along the section at 44.7°S and between -62 and -57°W is displayed in dark grey. (c) As panel (a) for the meridional velocity at M11 (grey and black lines) and altimetry at that location (blue).

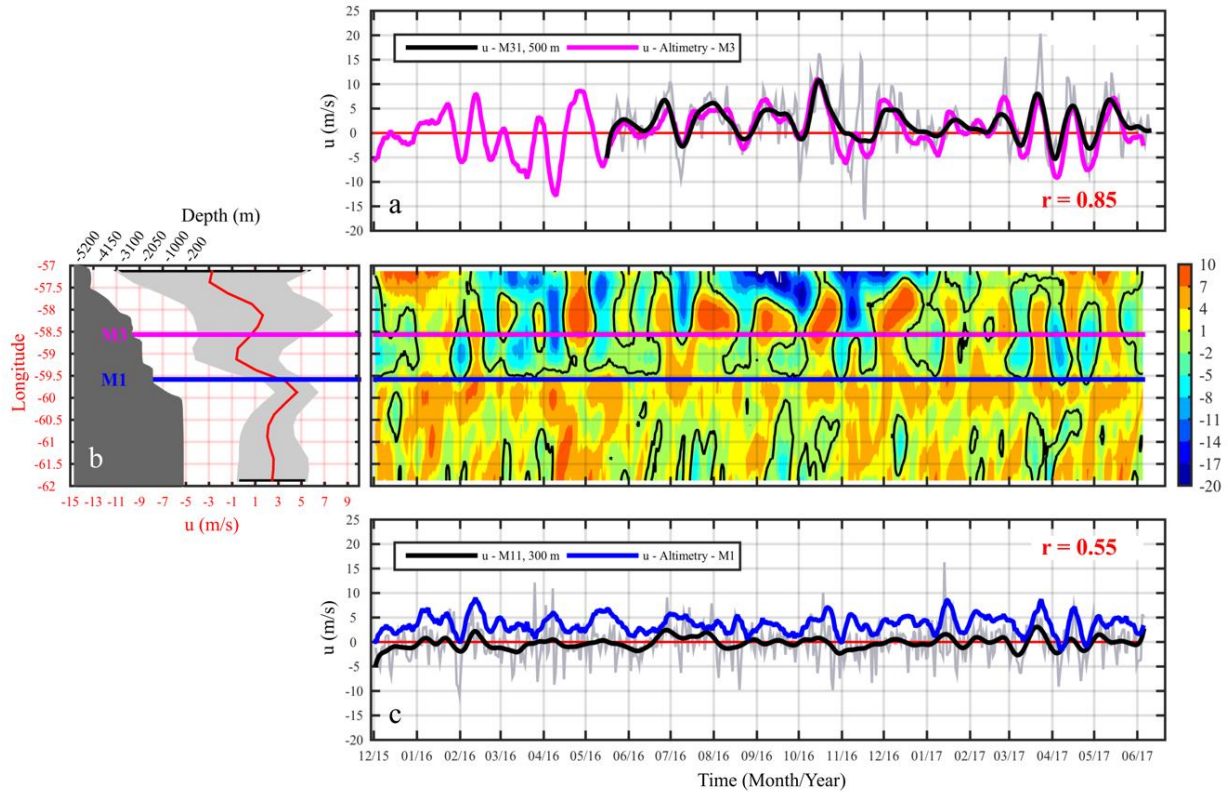


Figure 7. (a) In situ time series of the 2 and 20 days low-pass filtered daily resampled zonal velocity component at M31 are indicated with grey and black lines, respectively. The magenta line shows the time series of the zonal component of the surface velocity derived from satellite altimetry near M3. Correlation between the 20-day low pass filtered in situ time series and the altimeter time series is indicated in the bottom right corner. (b) Right panel: Longitude vs time plot of the meridional component of the current derived from satellite altimetry along 44.7°S and between 62 and 57°W. The blue (magenta) line represent the longitude of M1 (M3). Left panel: mean (red) and standard deviations (grey shading) of the zonal velocity derived from the altimeter. The topography along the section at 44.7°S and between -62 and -57 °W is displayed in dark grey. (c) As panel (a) for the zonal velocity at M11 (grey and black lines) and altimetry at that location (blue).

1
2
3
4
5
6
7
8
9
10
11
12
13
14
15
16
17
18
19
20
21
22
23
24
25
26
27
28
29
30
31
32
33
34
35
36
37
38
39
40
41
42
43
44
45
46
47
48
49
50
51
52
53
54
55
56
57
58
59
60
61
62
63
64
65

484

485 3.2.3. Relationship between the Malvinas Current and sea level anomaly

486 Sea level anomaly (SLA) maps show that mesoscale structures pass nearby or in-between the
487 moorings and have a significant impact on the observed velocity variability. To illustrate this
488 interaction, a sequence of SLA maps is displayed in Figure 8. On April 29, 2017 an anticyclonic
489 eddy with an amplitude of 18.2 cm and 85 km mean radius is observed between M1 and M3 (Figure
490 8a). Hereinafter we refer to this eddy as Matias. The positive SLA at the eddy core induces
491 anticyclonic circulation. The location of Matias on April 29, 2017, should decrease the strength of
492 the equatorward flow at M1 and increase it at M3. This is in agreement with the meridional velocity
493 variations derived from in situ observations (Figures 6a and 6c). To determine the origin of Matias
494 we identified and followed the positive SLA in previous SLA maps (Figure 8b-h). This suggests
495 that Matias was originated from two distinct positive SLA anomalies located near 53°W over the
496 Malvinas Plateau in early February 2017 (Figure 8h). These features appear to merge in early
497 March and subsequently displace westward and northward approximately following the isobath
498 orientations and eventually reaching the mooring array in late April (Figure 8f-a). The latter
499 observation suggests that a fraction of the along-isobath velocity variability is due to the
500 downstream propagation of mesoscale features. To determine at which location along the moorings
501 the SLA variations had the most significant impact, we computed the correlation between the SLA
502 along 44.7°S and the meridional velocity at M11 (300 m depth; Figure 9a) and at M31 (500 m
503 depth; Figure 9b), respectively. Results shows that the variability of the MC observed at M11 and
504 M31 is dominated by the SLA centered east of each mooring location. The highest correlation
505 between SLA and the meridional velocity at M11 (M31) was found 30 (40) km east of the mooring
506 location . In the following, we refer to the locations where we found the highest correlation
507 between SLA and the meridional velocity at M11 and at M31 as locations A (44.7°S; 59.1°W) and
508 B (44.7°S; 57.9°W), respectively (Figures 9a and 9b). Figure 9c (9d) shows the time series of the
509 along-slope velocity observed at M11 (M31) and the SLA time series obtained at A (B) location.
510 Figure 9a also suggests that the variability of the SLA over the shelf break (~60°W) does not affect
511 the meridional velocity at M1.

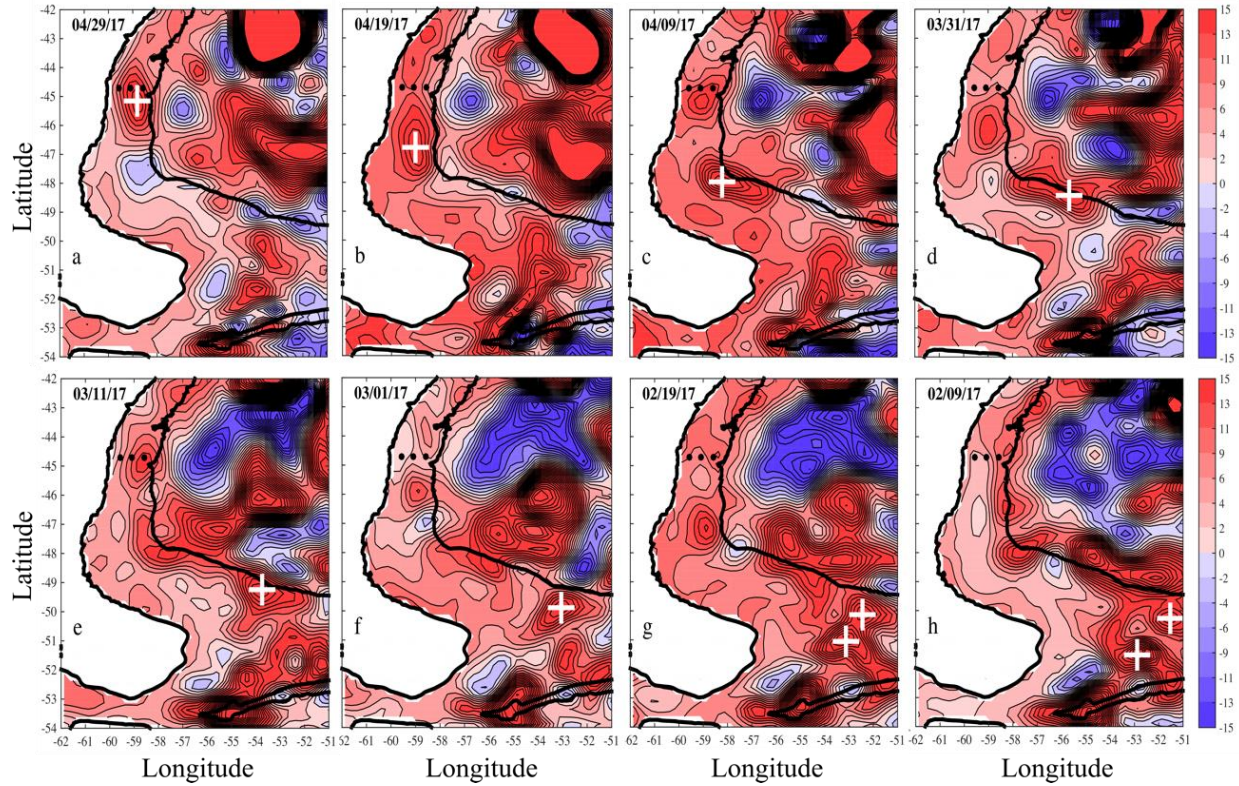


Figure 8. Distribution of sea level anomaly (SLA) between April 29, 2017 (a) and February 2, 2017 (h). Local maxima of positive SLA on the continental slope are indicated by a white cross. The 200 and 3000 m isobaths are indicated with black lines (GEBCO, (IOC, 2003)). The position of the moorings are indicated with black circles.

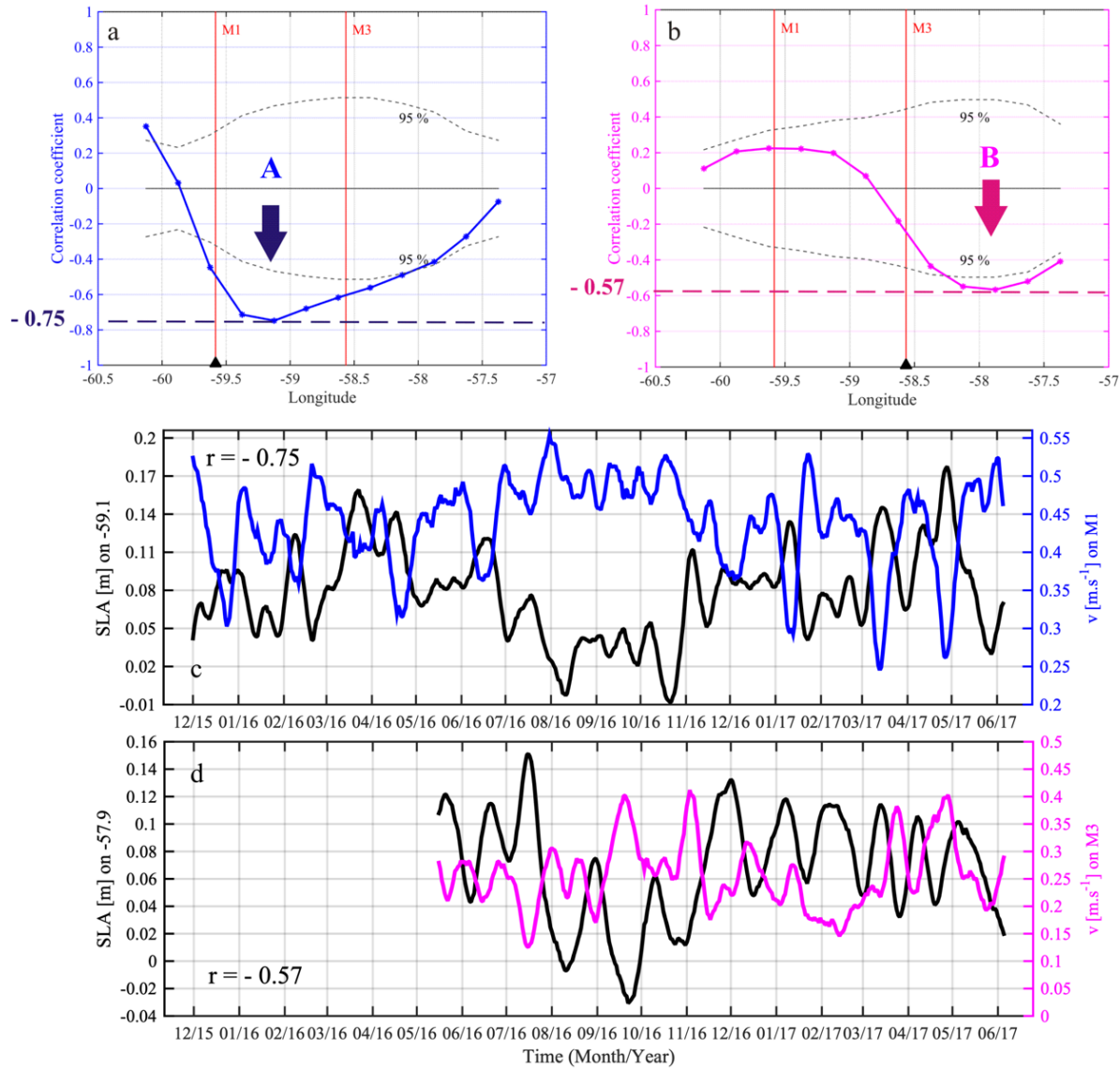


Figure 9. (a) Correlation between satellite-derived meridional velocity (v) close to M1 and SLA across the MC at 44.7°S. The position of the moorings M1 and M3 are indicated by vertical red lines. The black dashed lines indicate 95% confidence levels. (b) As in panel (a) for M3. (c) Time series of satellite derived meridional velocity (v) close to M1 (blue) and SLA (black) at the location of maximum correlation observed in panel (a) (44.7°S; 59.1°W). (d) Time series of satellite derived meridional velocity (v) close to M3 (magenta) and SLA (black) at the location of maximum correlation observed in panel (b) (44.7°S; 57.9°W).

1
2
3
4 5295
6 530 3.2.4. Propagation of SLA along the western slope of the Argentine Basin

7
8 531 In the previous section we showed that the variability of the MC observed at M1 and M3 at 44.7°S
9
10 532 is mostly affected by the SLA variability 30 km and 40 km east of the mooring locations
11
12 533 respectively. Here, we show that the main contributor of the SLA variability observed at those
13
14 534 locations (A and B) is due the presence of SLA that propagate northward through the array.
15
16 535 Assuming that the MC flows mainly along constant planetary potential vorticity (PV) contours
17
18 536 (e.g. Saraceno et al., 2004) we examined the SLA variability from December 2015 to June 2017
19
20 537 along the contours of constant PV that correspond to A and B locations (Figure 10). The PV
21
22 538 contour selected is $-2.9 \times 10^{-8} \text{ m}^{-1} \text{ s}^{-1}$ for A and $-5.2 \times 10^{-8} \text{ m}^{-1} \text{ s}^{-1}$ for B locations. The PV contours
23
24 539 selected correspond roughly to the 1950 m and 3500 m isobaths at 44.7°S (Figure 10a). These PV
25
26 540 contours run approximately parallel to each other along the western margin of the Argentine Basin,
27
28 541 but sharply diverge south of 49°S, with the $-2.9 \times 10^{-8} \text{ m}^{-1} \text{ s}^{-1}$ PV extending southward and westward
29
30 542 and the $-5.2 \times 10^{-8} \text{ m}^{-1} \text{ s}^{-1}$ PV running eastward along the northern flank of the Malvinas Plateau.
31
32 543 The slanted pattern of SLA anomalies along these paths (Figure 10b and 10c) are indicative that
33
34 544 those anomalies are propagating along the contours selected. So far the results show that the
35
36 545 propagation of SLA along the selected PV contours contribute to the meridional velocity
37
38 546 fluctuations observed at 44.7°S. We suggest that the SLA could be associated with the presence of
39
40 547 mesoscale structures (or eddies) that propagate along the Patagonian slope.

41 548
42
43 549 Furthermore, Figures 10b and 10c show that the SLA arriving at 44.7°S originates at different
44
45 550 locations. Figure 10b shows that most of the SLA that propagate along the PV from W1 to W2
46
47 551 (Figure 10a) originate in the northern flank of the North Scotia Ridge, at about (53.5°S, 56°W)
48
49 552 and, occasionally, at about 50°S and 53°W (Figures 10a and 10b). On the other hand, Figure 10c
50
51 553 shows that the majority of the SLA that propagate along the PV from E1 to E2 can be tracked up
52
53 554 to 49.6°S and 47.2°W and occasionally up to 49.3°S and 39.6°W, suggesting that the origin of these
54
55 555 SLA is along the Malvinas Escarpment, in the northern flank of the Malvinas Plateau. After
56
57 556 passing through the array, SLAs continue travelling northward along the slope until they dissipate
58
59 557 about around 40°S (Figure 10). The large amplitude of SLA observed north of 40°S is indicative
60
61 558 of the alternating impact of subtropical and subantarctic waters, characteristic of the encounter of
62
63
64
65

1
2
3
4
5
6
7
8
9
10
11
12
13
14
15
16
17
18
19
20
21
22
23
24
25
26
27
28
29
30
31
32
33
34
35
36
37
38
39
40
41
42
43
44
45
46
47
48
49
50
51
52
53
54
55
56
57
58
59
60
61
62
63
64
65

559 the Brazil and Malvinas Currents at the Confluence. These larger amplitude SLA fluctuations may
560 mask the northward propagation of SLA beyond the Confluence.

561
562 The mean phase speed propagation of the SLA was determined by the slope of slanted SLA pattern
563 displayed in Figures 10b and 10c. From 50°S to 40°S, the SBTW that propagate along the PV
564 contours from W1 to W2 are slightly faster (mean phase speeds = $0.17 \pm 0.02 \text{ m s}^{-1}$) than those
565 that propagate along the PV from E1 to E2 (mean phase speeds = $0.14 \pm 0.01 \text{ m s}^{-1}$). We also
566 observed that the SLA that propagate between W1 and E1 took ~2.5 months to reach the location
567 of the moorings from 50°S, (Figure 10). A similar time took Matias to reach 44.7°S from 50°S
568 (Figures 8a-f).

1
2
3
4
5
6
7
8
9
10
11
12
13
14
15
16
17
18
19
20
21
22
23
24
25
26
27
28
29
30
31
32
33
34
35
36
37
38
39
40
41
42
43
44
45
46
47
48
49
50
51
52
53
54
55
56
57
58
59
60
61
62
63
64
65

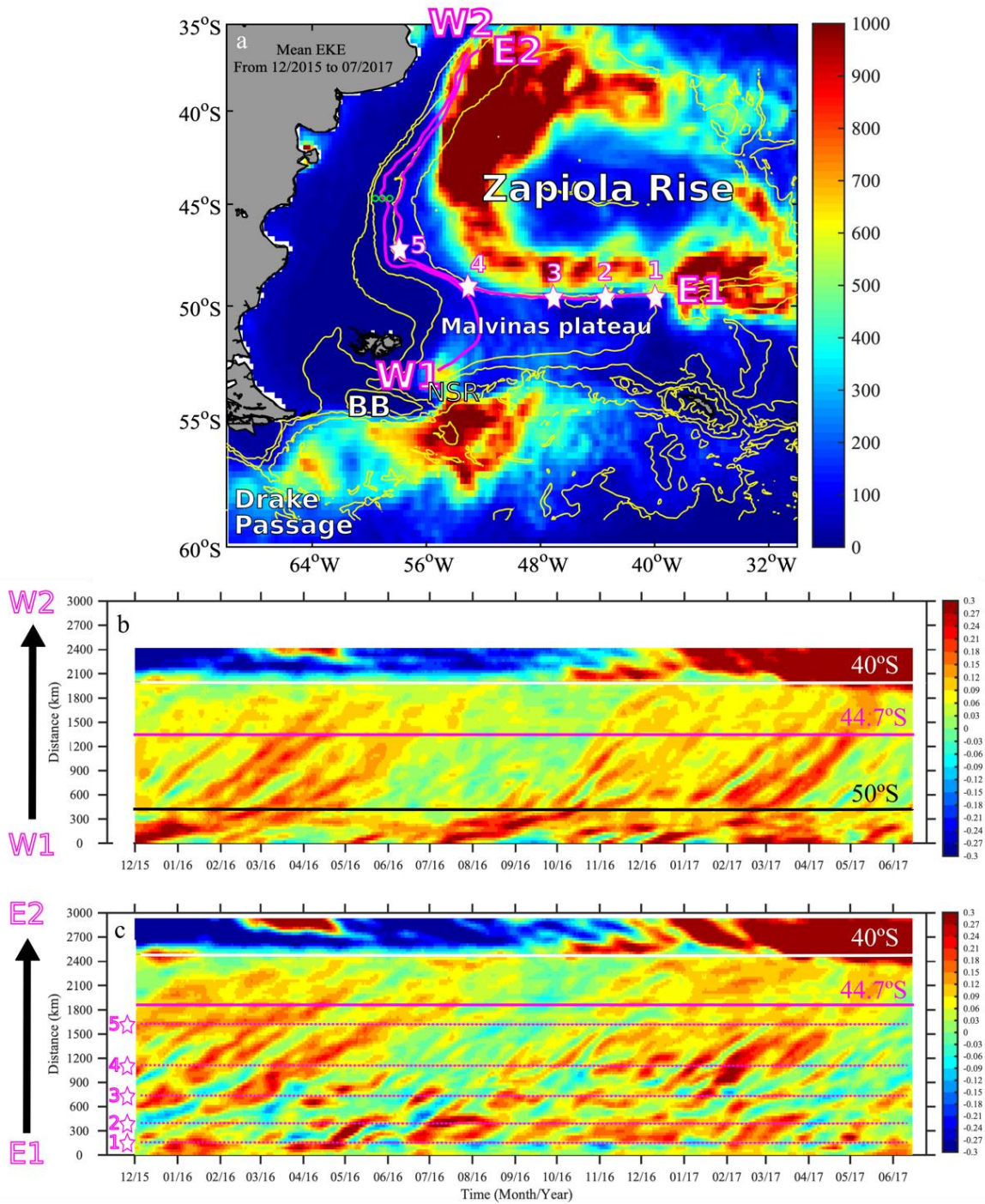


Figure 10. (a) Mean eddy kinetic energy (EKE) ($\text{cm}^2 \text{s}^{-2}$) derived from satellite-derived SLA between December 2015 and July 2017. Yellow contours indicate the 200, 1000, 3000 and 5000 m isobaths (GEBCO, (IOC, 2003)). The location of the North Scotia Ridge, Drake Passage, Malvinas Plateau, Zapiola Rise and Burdwood Bank (BB) are indicated. Magenta lines correspond

1
2
3
4 575 to contours of constant potential vorticity (PV) that passed over the maxima correlation points
5
6 576 indicated in Figure 9. The five white stars located on the PV from E1 to E2 indicate distances from
7
8 577 E1. From the 1st to the 5th star, the distances from E1 are: 110, 400, 690, 1100 and 1580 m. The
9
10 578 green circles indicate the location of the moorings. (b) Distance vs time plot of SLA along the
11
12 579 constant PV line from W1 to W2 indicated in panel (a). The magenta line indicates the latitude of
13
14 580 the mooring's location. The y-axis shows the distance from south to north (in km). (c) As in (b)
15
16 581 but for the constant potential vorticity line from E1 to E2 in panel (a). The five magenta dashed
17
18 582 lines denote the distances from "E1" indicated by stars in panel (a).
19
20
21
22
23
24
25
26
27
28
29
30
31
32
33
34
35
36
37
38
39
40
41
42
43
44
45
46
47
48
49
50
51
52
53
54
55
56
57
58
59
60
61
62
63
64
65

584

585

586

587

588

589

590

591

592

593

594

595

596

597

598

599

600

601

602

603

604

605

1
2
3
4
5
6
7
8
9
10
11
12
13
14
15
16
17
18
19
20
21
22
23
24
25
26
27
28
29
30
31
32
33
34
35
36
37
38
39
40
41
42
43
44
45
46
47
48
49
50
51
52
53
54
55
56
57
58
59
60
61
62
63
64
65

606 To further explore the SLA along the western slope of the Argentine Basin, we tracked the SLA
607 variability along five additional PV contours that correspond to the 550, 1100, 1400, 2450 and
608 2750 m isobaths at 44.7°S (Figure S14 and S15 a-g). Results show that there are SLA that
609 propagate northward along all the selected PV contours and that their phase speeds decrease in the
610 offshore direction from $0.21 \pm 0.04 \text{ m s}^{-1}$ to $0.14 \pm 0.01 \text{ m s}^{-1}$ (Figure S15 b-g). On the other hand,
611 the vertical lines observed in the Hovmöller diagram of the SLA along the PV contour of $-20 \cdot 10^{-8}$
612 $\text{m}^{-1} \text{ s}^{-1}$ (500 m isobath at 47°S, Figure S15a) are associated with the propagation of fast SLA which
613 are only observed along the upper portion of the slope. The propagation speed of these fast SLA
614 cannot be resolved with the available altimetry data.

615
616 Finally, taking advantage of the availability of the satellite altimetry data, we extended the analysis
617 of the SLA along the PV contours from 1993 to 2017. We find a pattern similar to the one obtained
618 during the December 2015 - July 2017 period: SLA propagating northward along the slope (Figure
619 S16). A spectral analysis of the 24 years SLA time series extracted at A and B locations (Figures
620 9a and 9b) show significant peaks at a near-annual time scale and between 25 and 140 days at both
621 locations (Figure 11).

622
623
624

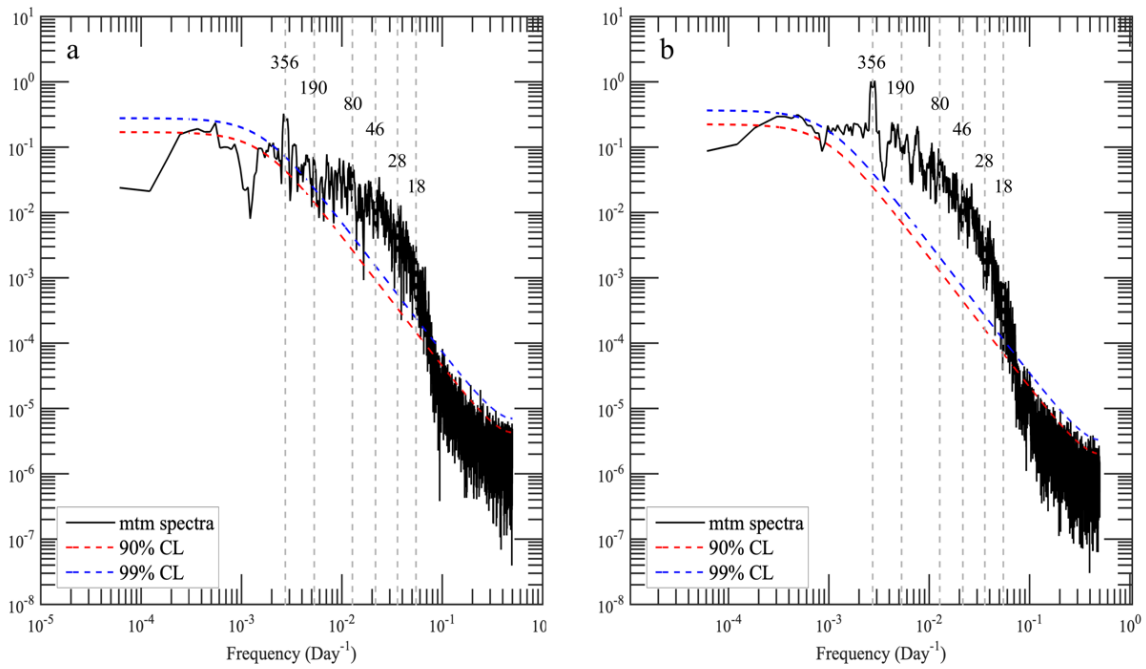


Figure 11. Spectra (m^2/cpd) of the SLA time series at the intersection of 44.7°S with the constant PV = $-5.2 \cdot 10^{-8} \text{ m}^{-1} \text{ s}^{-1}$ (a) and PV = $-2.9 \cdot 10^{-8} \text{ m}^{-1} \text{ s}^{-1}$ (b). Vertical dashed lines and numbers indicate significant periodicities in days.

4 Discussion

The MC has been studied from observations during the past 30 years around 41°S. At that latitude, the proximity of the Brazil-Malvinas Confluence severely impacts the time variability of the MC (Ferrari et al., 2017). The observations described here, collected at 44.7°S, provide the first evaluation of the MC variability away from the complexity introduced by the Confluence.

Mean velocities at M1, M2_a and M3 suggest that the MC has an equivalent-barotropic structure and flows parallel to the isobaths along the continental shelf break at 44.7°S, in good agreement with previous estimates based on hydrographic (Piola and Gordon, 1989) and current meter observations further north (Vivier and Provost, 1999a; Ferrari et al., 2017; Paniagua et al., 2018). In a few occasions, the equatorward surface velocities of the MC decreased up to a 30% relative to their time averaged means (Figure 6c). The largest decreases in meridional velocity occur when eddies interact with the MC, strongly modifying the velocity structure of the MC. Similar events were reported by Artana et al., (2016) at these latitudes.

The analysis of the SLA revealed (i) that the MC variability at M1 and M3 locations is partially due to the presence of SLAs that propagate northward along the continental slope and (ii) the regions from where the SLAs originate. From West to East, the phase speed of the SLA decrease from $0.21 \pm 0.04 \text{ m s}^{-1}$ to $0.14 \pm 0.01 \text{ m s}^{-1}$. A decrease in phase speed can be associated with a decrease in the bottom slope (Gill, 1982). In our region it is difficult to estimate the bottom slope, given the complexity of the bathymetry (Figure 2). Yet, without considering the small canyons it is right to assume that the bottom slope decreases eastwards and therefore provides a possible explanation for the decrease in the phase speed observed according to Gill (1982). Fu (2006), used the generic term “eddies” to represent the various forms of mesoscale SLAs and estimated similar phase speeds ($\sim 0.12 \text{ m s}^{-1}$) for the propagation of eddies along the Patagonian slope between 50°S to 45°S. Our results suggest that the passage of such SLAs affect the MC meridional velocities at 44.7°S. The propagation of SLAs that we are observing are much slower than the coastally trapped waves that have been reported along the Patagonian shelf break and that have been associated with Kelvin waves propagating from the equatorial Pacific (Clarke and Ahmed, 1999; Vivier et al., 2001; Cravatte et al., 2003; Artana et al., 2016; Combes and Matano, 2019).

1
2
3
4
5
6
7
8
9
10
11
12
13
14
15
16
17
18
19
20
21
22
23
24
25
26
27
28
29
30
31
32
33
34
35
36
37
38
39
40
41
42
43
44
45
46
47
48
49
50
51
52
53
54
55
56
57
58
59
60
61
62
63
64
65

675 We showed that the MC is affected by SLA, such eddies and filaments, that propagate along the
676 continental slope. The interaction between western boundary currents and propagating mesoscales
677 features has been documented also in other places. For example, in the North Atlantic,
678 the variability of the deep western boundary current (DWBC) is also affected by meanders and
679 eddies (Biló and John, 2020) that are probably generated by westward propagating Rossby wave-
680 like perturbations (Meinen and Garzoli, 2014; Biló and John's, 2020).

681
682 A significant 25-day periodicity is revealed by the spectra of the zonal velocity at M3 (EOF2 of
683 M3, Figure S11d). Based on the the analysis of SLA variability, Fu et al. (2001) reported the
684 existence of topographic Rossby waves with a period close to 25 days that propagate around the
685 Zapiola Rise, a sedimentary elevation about 1200 m in height, centered at 43°W-45°S (Figure 10a).
686 Fu (2007) provided further evidence of the interaction between the large 25-day waves and the
687 energetic mesoscale variability in the Argentine basin. These observations suggest that the 25-day
688 peak that characterizes the zonal currents at M3 may be due to the barotropic topographic Rossby
689 waves described by Fu et al. (2001) that reach the east side of the MC, close to M3 location (Figure
690 10a).

691
692 SLA variations that modulate the intensity of the MC at 44.7°S can be tracked upstream to the
693 northern flank of the North Scotia Ridge at about 53.5°S and 56°W and to the northern flank of the
694 Malvinas Plateau, along the Malvinas Escarpment (Figure 10). These regions coincide with local
695 maxima of eddy kinetic energy in the Southwestern Atlantic (Figure 10a). Several studies suggest
696 that these regions of large eddy kinetic energy are associated with the interaction of the flow with
697 the complex bottom topography (Fu, 2006; Fetter and Matano, 2008; Saraceno and Provost, 2012;
698 Artana et al., 2016; Mason et al., 2017). Our analyses suggest that these regions are likely sources
699 of SLAs that propagate in forms of mesoscale structures (or eddies) along the Patagonian slope
700 and modulate the strength of the MC. The estimated propagation velocity and origin of the SLAs
701 derived in this study are in agreement with recent analyses of a numerical model (Poli et al., 2020).

702
703
704
705

1
2
3
4
5
6
7
8
9
10
11
12
13
14
15
16
17
18
19
20
21
22
23
24
25
26
27
28
29
30
31
32
33
34
35
36
37
38
39
40
41
42
43
44
45
46
47
48
49
50
51
52
53
54
55
56
57
58
59
60
61
62
63
64
65

706

707

5 Summary of conclusions

18-months of in situ current observations over the western slope of the Argentine Basin at 44.7°S show mean northward velocities up to $37 \pm 9.7 \text{ cm s}^{-1}$ at 300 m depth. The in situ meridional velocities observed 80 km apart are not correlated due the presence of mesoscale features within the Malvinas Current. The flow is vertically coherent up to 1500 m depth both in M1 and M3. The 20-day low pass filtered in situ and satellite-derived meridional velocities are significantly correlated (~ 0.8), suggesting that the latter is a good proxy to monitor currents variations at time scales longer than 20 days. The variations in the intensity of the Malvinas Current at 44.7°S are modulated by variations in sea-level anomaly that originate in the northern flank of the North Scotia Ridge (53.5°S, 56°W) and along the Malvinas Escarpment ($\sim 50^\circ\text{S}$, 47.2-39.6°W). The anomalies propagate northward closely following lines of constant potential vorticity. The SLA reaching the onshore flank of the Malvinas Current along the upper slope originate mostly from the northern flank of the North Scotia Ridge, while those arriving at the offshore flank originate along the northern edge of the Malvinas Plateau near 40°W. The SLA that propagate along the offshore flank are slower than those that propagate along the onshore flank of the MC.

723

724

725

726

727

728

729

730

731

732

733

734

735

1
2
3
4
5
6
7
8
9
10
11
12
13
14
15
16
17
18
19
20
21
22
23
24
25
26
27
28
29
30
31
32
33
34
35
36
37
38
39
40
41
42
43
44
45
46
47
48
49
50
51
52
53
54
55
56
57
58
59
60
61
62
63
64
65

Acknowledgments, Samples, and Data

A large number of people helped collecting the in situ data that are the core of the results presented here. The cruises were performed with the collaboration of the offshore rescue vessel SB-15 Tango (Prefectura Naval Argentina) and R/V Puerto Deseado (Consejo Nacional de Investigaciones Científicas y Tecnológicas). The cruises carried out with the offshore rescue vessel SB-15 Tango and the R/V Puerto Deseado were financed by Prefectura Naval Argentina and Servicio de Hidrografía Naval, respectively. We particularly thank the support of the following institutions: SHN, Mincyt, INIDEP, CONICET, UBA, Prefectura Naval Argentina, Puerto Deseado crew, CNRS, Sorbonne Université LOCEAN, LOPS and DT-INSU. This study is a contribution to EUMETSAT/CNES DSP/OT/07-2118 and DSP/OT/07-4571, CONICET-FYPF PIO 133-20130100242. Additional support was provided by grant CRN3070 from the Inter-American Institute for Global Change Research through NSF grant GEO-1128040. GFP benefited from doctoral scholarship from CONICET, Argentina. Satellite data are available at Copernicus Marine Environment monitoring service (CMEMS) (<http://marine.copernicus.eu/>). In situ data are available at SEANOE (www.seanoe.org cf reference below Saraceno et al., 2020).

1
2
3
4
5
6
7
8
9
10
11
12
13
14
15
16
17
18
19
20
21
22
23
24
25
26
27
28
29
30
31
32
33
34
35
36
37
38
39
40
41
42
43
44
45
46
47
48
49
50
51
52
53
54
55
56
57
58
59
60
61
62
63
64
65**References**

- 767 Acha, E. M., H. W. Mianzan, R. A. Guerrero, M. Favero, and J. Bava (2004), Marine fronts at
768 the continental shelves of austral South America - Physical and ecological processes, *J.*
769 *Mar. Syst.*, *44*, 83–105.
- 770
771 Artana, C., R. Ferrari, Z. Koenig, M. Saraceno, A. R. Piola, and C. Provost (2016). Malvinas
772 Current variability from Argo floats and satellite altimetry, *J. Geophys. Res. Oceans*, *121*,
773 4854– 4872, doi:10.1002/2016JC011889
- 774 Beron-Vera, F. J., Bodnariuk, N., Saraceno, M., Olascoaga, M. J., and Simionato, C. (2020).
775 Stability of the Malvinas Current. *Chaos: An Interdisciplinary Journal of Nonlinear*
776 *Science*, *30*(1), 013152.
- 777 Biló, T. C. and Johns, W. E. (2020). The Deep Western Boundary Current and Adjacent Interior
778 Circulation at 24°–30°N: Mean Structure and Mesoscale Variability. *Journal of Physical*
779 *Oceanography*, *50*(9), 2735-2758.
- 780 Carranza, M. M., Gille, S. T., Piola, A. R., Charo, M., and Romero, S. I. (2017). Wind
781 modulation of upwelling at the shelf-break front off Patagonia: Observational evidence, *J.*
782 *Geophys. Res. Oceans*, *122*, 2401–2421, doi:10.1002/2016JC012059
- 783 Clarke, A. J., and Ahmed, R. (1999). Dynamics of remotely forced intraseasonal oscillations off
784 the western coast of South America. *J. Phys. Oceanogr.*, *29*, 240–258.
- 785 Cravatte, S., Picaut, J., Eldin, G., (2003). Second and first baroclinic kelvin modes in the
786 equatorial pacific intraseasonal timescales. *J. Geophys. Res.* *108* (C8), 3266, <http://dx.doi.org/10.1029/2002JC001511>
- 787
788 Combes, V., and Matano, R. P. (2014). A two- way nested simulation of the oceanic circulation
789 in the Southwestern Atlantic. *Journal of Geophysical Research: Oceans*, *119*(2), 731-756.
790 [https://doi.org/ 10.1002/2013JC009498](https://doi.org/10.1002/2013JC009498)
- 791 Combes, V., and Matano, R. P. (2019). On the origins of the low-frequency sea surface height
792 variability of the Patagonia shelf region. *Ocean Modelling*, *142*, 101454.
- 793 Dickson. R. R., Gurbutt, P. A., and Pillai, V. N. (1980). Satellite evidence of enhanced
794 upwelling along the European continental slope. *J. Phys. Oceanogr.* *10*, 813-819.
- 795 Ferrari, R., Provost, C., Renault, A., Sennéchaël, N., Barré, N., Park, Y. H., and Lee, J. H.
796 (2012). Circulation in Drake Passage revisited using new current time series and satellite
797 altimetry: 1. The Yaghan Basin. *Journal of Geophysical Research: Oceans*, *117*(C12).

- 1
2
3
4 798 Ferrari, R., Artana, C., Saraceno, M., Piola, A. R., and Provost, C. (2017). Satellite altimetry and
5
6 799 current-meter velocities in the Malvinas Current at 418S: Comparisons and modes of
7
8 800 variations. *Journal of Geophysical Research: Oceans*, *122*, 9572–9590.
9
10 801 <https://doi.org/10.1002/2017JC013340>
- 11 802 Fetter, A. F. H., and Matano, R. P. (2008). On the origins of the variability of the Malvinas
12
13 803 Current in a global, eddy-permitting numerical simulation, *J. Geophys. Res.*, *113*, C11018,
14
15 804 doi:10.1029/2008JC004875
- 16
17 805 Fournier. R. O., van Det, M., Wilson, J. S., and Hargreaves, N. B. (1979). Influence of the shelf-
18
19 806 break front off Nova Scotia on phytoplankton standing stock in winter. *J. Fish. Res. Board*
20
21 807 *Can.* *36*, 1228-1237.
- 22 808 Franco, B. C., Piola, A. R., Rivas, A. L., Baldoni, A., and Pisoni, J. P. (2008). Multiple thermal
23
24 809 fronts near the Patagonian shelf break, *Geophys. Res. Lett.*, *35*, L02607,
25
26 810 doi:10.1029/2007GL032066.
- 27
28 811 Franco, B. C., Palma, E. D., Combes, V., and Lasta, M. L. (2017). Physical processes controlling
29
30 812 passive larval transport at the Patagonian Shelf Break Front. *Journal of Sea Research*, *124*,
31
32 813 17-25.
- 33 814 Frey, D. I., Piola, A. R., Krechik, V. A., Fofanov, D. V., Morozov, E. G., Silvestrova, K. P., Tarakanov,
34
35 815 R. Y., and Gladyshev, S. V. (2020). Direct measurements of the Malvinas Current velocity
36
37 816 structure, submitted to *J. Geophys. Res. Oceans*.
- 38 817 Fu, L.-L., Cheng, B., and Qiu, B. (2001). 25-day period large-scale oscillations in the Argentine
39
40 818 Basin revealed by the TOPEX/Poseidon altimeter. *J. Phys. Oceanogr.*, *31*, 506–517.
- 41
42 819 Fu, L.-L. (2006). Pathways of eddies in the South Atlantic Ocean revealed from satellite
43
44 820 altimeter observations. *Geophys. Res. Lett.*, *33*, L14610, doi:10.1029/2006GL026245
- 45
46 821 Fu, L.-L., (2007). Interaction of mesoscale variability with large-scale waves in the Argentine
47
48 822 Basin. *J. Phys. Oceanogr.*, *37*, 787 – 793, doi:10.1175/JPO29911
- 49
50 823 Garzoli, S. L., and Matano, R. (2011). The South Atlantic and the Atlantic meridional
51
52 824 overturning circulation. *Deep-Sea Research Part II*, *58*(17), 1837-1847.
- 53 825 Ghil, M., Allen, R. M., Dettinger, M. D., Ide, K., Kondrashov, D., Mann, M. E., Robertson A.,
54
55 826 Saunders, A., Tian, I., Varadi, F., and Yiou, P. (2002). Advanced spectral methods for
56
57 827 climatic time series. *Reviews of geophysics*, *40*(1), 3-1.
58
59
60
61
62
63
64
65

- 1
2
3
4 828 Gill, A. E. (1982). The Tropics, In William L. Donn (Ed.), *Atmosphere-Ocean dynamics* (Vol.
5
6 829 30, pp. 429-457). San Diego, International Geophysics Series.
7
8 830 IOC, IHO, and BODC (2003). “Centenary Edition of the GEBCO Digital Atlas”, published on
9
10 831 CD-ROM on behalf of the Intergovernmental Oceanographic Commission and the
11
12 832 International Hydrographic Organization as part of the General Bathymetric Chart of the
13
14 833 Oceans; British Oceanographic Data Centre, Liverpool.
15 834 Lastras, G., Acosta, J., Muñoz, A., and Canals, M. (2011). Submarine canyon formation and
16
17 835 evolution in the Argentine Continental Margin between 44°30’S and 48°S.
18
19 836 *Geomorphology*, 128, 116–136, doi:10.1016/j.geomorph.2010.12.027.
20
21 837 Lutz, V. A., Segura, V., Dogliotti, A. I., Gagliardini, D. A., Bianchi, A. A., and Balestrini, C. F.
22
23 838 (2010). Primary production in the Argentine Sea during spring estimated by field and
24
25 839 satellite models. *Journal of Plankton Research*, 32(2), 181-195.
26 840 Martinetto, P., Alemany, D., Botto, F. *et al.* (2020). Linking the scientific knowledge on marine
27
28 841 frontal systems with ecosystem services. *Ambio* (49), 541–556.
29
30 842 <https://doi.org/10.1007/s13280-019-01222-w>
31
32 843 Mason, E., Pascual, A., Gaube, P., Ruiz, S., Pelegrí, J. L., and Delepoulle A. (2017). Subregional
33
34 844 characterization of mesoscale eddies across the Brazil-Malvinas Confluence. *J. Geophys.*
35
36 845 *Res.Oceans*, 122, 3329–3357, doi:10.1002/2016JC012611
37 846 Matano, R. P., and Palma, E. D. (2008). On the upwelling of downwelling currents. *Journal of*
38
39 847 *Physical Oceanography*, 38, 2482–2500. <https://doi.org/10.1175/2008JPO3783.1>
40
41 848 Mazé, R., Camus, Y., and Le Tareau, J. Y. (1986). Formation de gradients thermiques à la
42
43 849 surface de l’océan, au-dessus d’un talus, par interaction entre les ondes internes et le
44
45 850 mélange dû au vent. *ICES Journal of Marine Science*, 42(3), 221-240.
46 851 Meinen, C. S., and Garzoli, S. L. (2014). Attribution of deep western boundary current
47
48 852 variability at 26.5°N. *Deep-Sea Res.*, 90, 81–90, <https://doi.org/10.1016/j.dsr.2014.04.016>.
49
50 853 Paniagua, G. F., Saraceno, M., Piola, A. R., Guerrero, R., Provost, C., Ferrari, R., et al. (2018).
51
52 854 Malvinas Current at 40°S–41°S: First assessment of temperature and salinity temporal
53
54 855 variability. *Journal of Geophysical Research: Oceans*, 123. [https://doi.org/](https://doi.org/10.1029/2017JC013666)
55
56 856 [10.1029/2017JC013666](https://doi.org/10.1029/2017JC013666).
57
58
59
60
61
62
63
64
65

- 1
2
3
4 857 Peterson, R.G., and Whitworth III, T. (1989). The Subantarctic and Polar Fronts in relation to
5
6 858 deep water masses through the southwestern Atlantic. *Journal of Geophysical Research:*
7
8 859 *Oceans*, 94(C8), 10817-10838.
- 9
10 860 Peterson, R. G., and Stramma, L. (1991). Upper-level circulation in the South Atlantic
11
12 861 Ocean. *Progress in oceanography*, 26(1), 1-73.
- 13
14 862 Piola, A. R., and Gordon, A. L. (1989). Intermediate Waters in the Southwest South-Atlantic,
15
16 863 *Deep-Sea Res., Part I*, 36(1), 1–16, doi:10.1016/ 0198-0149(89)90015-0.
- 17 864 Piola, A. R., Franco, B. C., Palma, E. D., and Saraceno, M. (2013). Multiple jets in the Malvinas
18
19 865 Current, *J. Geophys. Res. Oceans*, 118, 2107–2117, doi:10.1002/jgrc.20170.
- 20
21 866 Podesta, G. P. (1990). Migratory pattern of Argentine hake *Merluccius hubbsi* and oceanic
22
23 867 processes in the Southwestern Atlantic Ocean. *Fishery Bulletin*, 88(1), pp.167-177.
- 24
25 868 Poli, L., Artana, C., Provost, C., Sirven, J., Sennéchaël, N., Cuypers, Y., and Lellouche, J. M.
26
27 869 (2020). Anatomy of subinertial waves along the Patagonian shelf break in a 1/12° global
28
29 870 operational model. *Journal of Geophysical Research: Oceans*, e2020JC016549.
- 30 871 Rattray, M. (1960). On the coastal generation of internal tides. *Tellus*, 12, 54-62.
- 31
32 872 Romero, S. I., A. R. Piola, M. Charo, and C. A. E. Garcia (2006), Chlorophyll-a variability off
33
34 873 Patagonia based on SeaWiFS data, *J. Geophys. Res.*, 111, C05021,
35
36 874 doi:10.1029/2005JC003244.
- 37 875 Saraceno, M., Provost, C., Piola, A. R., Bava, J., and Gagliardini, A. (2004). Brazil Malvinas
38
39 876 Frontal System as seen from 9 years of advanced very high resolution radiometer data, *J.*
40
41 877 *Geophys. Res.*, 109, C05027, doi:10.1029/2003JC002127.
- 42
43 878 Saraceno, M., Provost, C., and Piola A. R. (2005). On the relationship between satellite-retrieved
44
45 879 surface temperature fronts and chlorophyll a in the western South Atlantic, *J. Geophys.*
46
47 880 *Res.*, 110(C11), C11016, doi:10.1029/2004JC002736.
- 48 881 Saraceno, M., and Provost, C. (2012). On eddy polarity distribution in the southwestern
49
50 882 Atlantic. *Deep Sea Research Part I: Oceanographic Research Papers*, 69, 62-69.
- 51
52 883 Saunders, P. M., and King, B. A. (1995). Bottom currents derived from a shipborne ADCP on
53
54 884 WOCE cruise A11 in the South Atlantic, *Journal of Geophysical Research*, 25(3), 329–
55
56 885 347.
- 57
58
59
60
61
62
63
64
65

1
2
3
4
5
6
7
8
9
10
11
12
13
14
15
16
17
18
19
20
21
22
23
24
25
26
27
28
29
30
31
32
33
34
35
36
37
38
39
40
41
42
43
44
45
46
47
48
49
50
51
52
53
54
55
56
57
58
59
60
61
62
63
64
65

886 Saraceno, M., Provost C., Piola, A., Guerrero, R., Ferrari, R., Paniagua G. F., Lago, L. S. and
887 Artana, C. (2020). Malvinas Current 2015-2017: Mooring velocities.
888 SEANOE. <https://doi.org/10.17882/76617>.
889 Spadone, A., and Provost, C. (2009). Variations in the Malvinas Current volume transport since
890 October 1992. *Journal of Geophysical Research*, 114, C02002.
891 <https://doi.org/10.1029/2008JC004882>
892 Valla, D., and Piola, A. R. (2015), Evidence of upwelling events at the northern Patagonian shelf
893 break, *J. Geophys. Res. Oceans*, 120, doi:10.1002/2015JC011002
894 Vivier, F., and C. Provost (1999a), Direct velocity measurements in the Malvinas Current, *J.*
895 *Geophys. Res.*, 104, 21083–21104.
896 Vivier, F., and Provost, C. (1999b). Volume transport of the Malvinas Current: Can the flow be
897 monitored by TOPEX/POSEIDON? *Journal of Geophysical Research*, 104, 21,105–
898 21,122.
899 Vivier, F., Provost, C., and Meredith, M. (2001). Remote and local forcing in the Brazil
900 Malvinas Region, *J. Phys. Oceanogr.*, 31, 892–913, doi: 10.1175/1520-0485.

906 **Tables**

907

908 **Table 1.** Mooring Locations.

Mooring name	Latitude (°S)	Longitude (°W)	Bottom depth (m)	Deployment date	Recovery date
Buoy	-44.7	-59.9	200	5/16/2016	6/7/2016
M1	-44.7	-59.6	1320	11/26/2015	6/8/2017
M2	-44.7	-59.1	1945	11/26/2016	6/9/2017
M3	-44.7	-58.6	2608	5/14/2016	6/10/2017

909

910 **Table 2.** Statistics of current meters measurements over the continental Patagonian shelf break
 911 between December 2015 and June 2017. M_{ij} denotes current meters at moorings M1, M2, and M3,
 912 i being the mooring number and j standing for the level from the surface (see Figure 2). Here, Θ
 913 is the angle in degrees of mean velocity direction relative to the geographical north, \mathbf{V} (cm s^{-1}) is
 914 the magnitude of the time-average velocity and v (cm s^{-1}) and u (cm s^{-1}) are the velocity
 915 components, σ is the standard deviation and unless otherwise specified, mean values are indicated.
 916 All statistic values are reported with an accuracy of 1 cm s^{-1} .

917

Mooring	M11	M12	M13	M22a	M23a	M24a	M22b	M23b	M24b	M31	M32	M33	M34
Depth (m)	300	760	1042	1016	1315	1720	1560	1865	2270	500	976	1486	2100
Days	552	528	554	31	31	31	520	520	520	390	390	390	390
V_{\max}	61	47	39	33	23	24	35	52	43	46	37	30	19
V	37	28	16	24	16	9	11	4	1	20	15	12	8
Θ	0	0	3	-5	6	0	14	31	-23	-1	-1	5	7
u	0	0	-1	-2	2	0	3	2	0	0	0	1	1
σu	3	4	3	3	3	5	4	7	10	5	4	4	3
v	37	27	16	24	16	9	10	4	0	20	15	12	8
σv	10	7	7	5	5	7	4	3	5	7	6	6	5

918

1
2
3
4
5
6
7
8
9
10
11
12
13
14
15
16
17
18
19
20
21
22
23
24
25
26
27
28
29
30
31
32
33
34
35
36
37
38
39
40
41
42
43
44
45
46
47
48
49
50
51
52
53
54
55
56
57
58
59
60
61
62
63
64
65

1
2
3
4 919 **Table 3.** Statistics of ADCP observations at the oceanographic buoy between May 16 and June 7,
5
6 920 2016 (see location in Figure 1 and Table 1). C_i denotes ADCP measurements, i denotes the level
7
8 921 measured from the surface. Here, Θ is the mean velocity direction (relative to the geographical
9
10 922 north), V (cm s^{-1}) is the magnitude of the time-average velocity and v (cm s^{-1}) and u (cm s^{-1}) are
11
12 923 the velocity components, σ is the standard deviation and unless otherwise specified, mean values
13
14 924 are indicated.

15 925

Mooring	Depth (m)	V_{\max}	V	Θ	u	σu	v	σv
C1	10	66	54	0	-1	6	51	7
C2	20	71	55	-1	-1	5	53	8
C3	30	70	55	-1	-1	5	52	8
C4	40	68	53	-1	-1	4	51	8
C5	50	70	54	-2	-2	4	51	8
C6	60	70	56	-3	-4	6	53	8
C7	70	66	51	0	0	4	48	7
C8	80	64	48	-2	-2	4	46	7
C9	90	61	43	-3	-2	4	40	7
C10	100	61	46	-2	-2	3	44	7
C11	110	60	46	-1	-1	3	44	7
C12	120	59	45	-1	-1	3	43	7
C13	130	57	44	-1	-1	3	42	7
C14	140	55	41	-1	-1	3	39	6
C15	150	57	41	-25	0	4	39	7
C16	160	57	40	23	1	4	38	6
C17	170	55	39	1	1	4	36	6
C18	180	55	38	-2	1	4	35	7
C19	190	35	23	-41	2	3	21	5
C20	200	14	8	-15	-1	1	7	3

60 926

61
62
63
64
65

1
2
3
4
5
6
7
8
9
10
11
12
13
14
15
16
17
18
19
20
21
22
23
24
25
26
27
28
29
30
31
32
33
34
35
36
37
38
39
40
41
42
43
44
45
46
47
48
49
50
51
52
53
54
55
56
57
58
59
60
61
62
63
64
65

Table 4. Statistics of satellite derived velocities at the points closest to M1 and M3 (see locations in Figure 1 and Table 1). Here, Θ is the mean velocity direction (relative to the true north), V (cm s^{-1}) is the magnitude of the time-average velocity, σ is the standard deviation and v (cm s^{-1}) and u (cm s^{-1}) are the velocity components.

	M1	M3
Days	552	390
V_{\max} (cm s^{-1})	55	42
V (cm s^{-1})	44	26
Θ	5	2
u (cm s^{-1})	4	1
σu (cm s^{-1})	2	4
v (cm s^{-1})	44	26
σv (cm s^{-1})	6	6

932
933
934

Supporting Information for

**Malvinas Current at 44.7°S: First assessment of velocity temporal variability from
in situ data**

**Guillermina F. Paniagua^{1,2,3}, Martin Saraceno^{1,2,3}, Alberto R. Piola^{2,3,5}, Marcela
Charo⁵, Ramiro Ferrari^{1,2,3}, Camila Artana⁶ and Christine Provost⁴**

¹ Centro de Investigaciones del Mar y la Atmósfera (CIMA/CONICET-UBA), Ciudad
Autónoma de Buenos Aires, Argentina

² Departamento de Ciencias de la Atmósfera y los Océanos, Facultad de Ciencias
Exactas y Naturales, Universidad de Buenos Aires, Buenos Aires, Argentina

³ Unidad Mixta Internacional-Instituto Franco-Argentino para el Estudio del Clima y sus
Impactos (UMI-IFAECI/CNRS-CONICET-UBA), Buenos Aires, Argentina

⁴ Laboratoire d'Océanographie et du Climat: Experimentation et Approches Numériques
(LOCEAN), UMR 7159, Paris, Francia

⁵ Departamento de Oceanografía, Servicio de Hidrografía Naval (SHN), Buenos Aires,
Argentina

⁶ MERCATOR OCEAN, Parc Technologique du Canal, Ramonville Saint Agne, France

Corresponding author: Guillermina F. Paniagua
(guillermina.paniagua@cima.fcen.uba.ar)

Contents of this file

- Figures and their captions from S1 to S16:

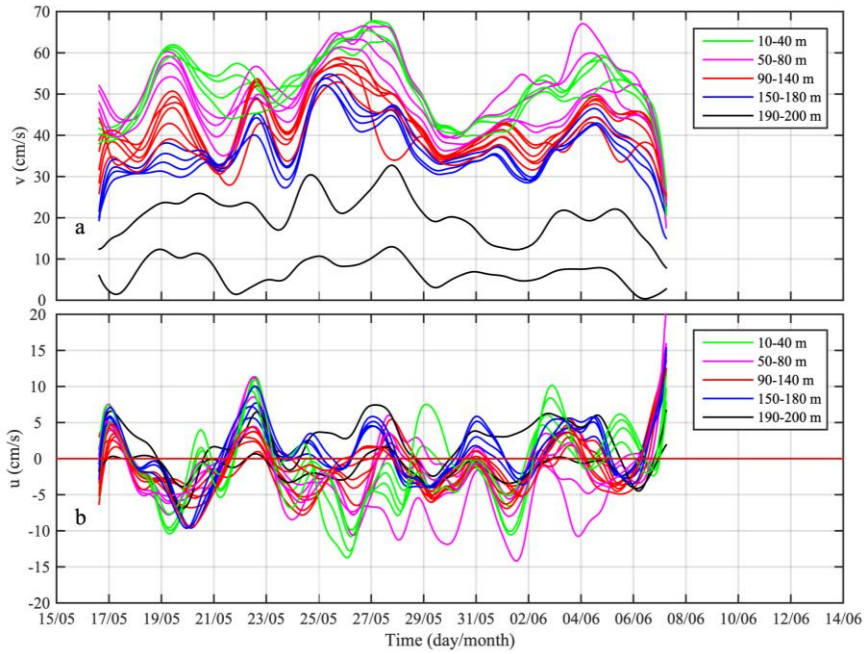


Figure S1. In situ time series of meridional (a) and zonal (b) velocities recorded by the oceanographic buoy at different depths.

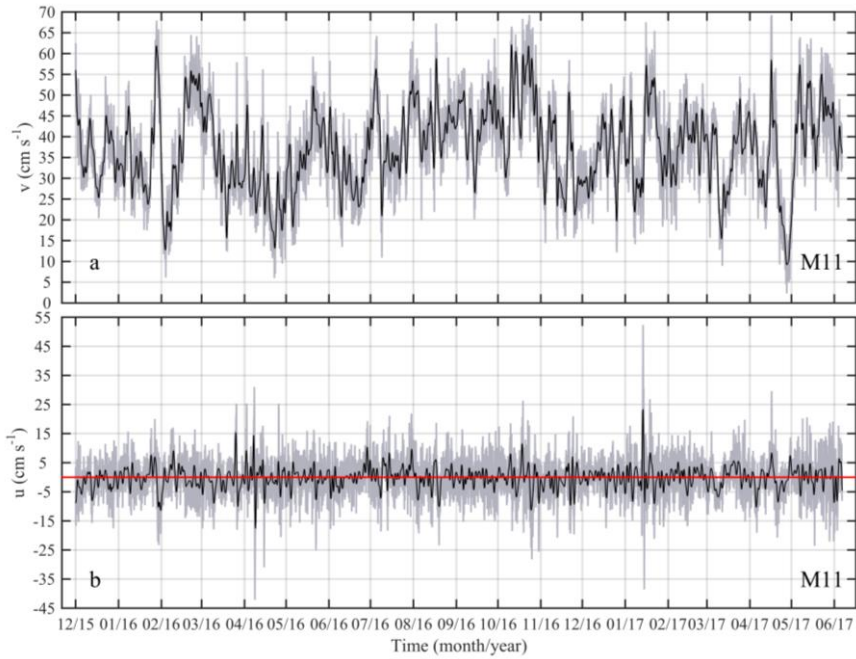


Figure S2. In situ time series of meridional (a) and zonal (b) velocities at M11 (mooring M1, 300 m). Light-gray lines correspond to raw data while black bold lines correspond to 48 h low-pass filtered data. Horizontal red lines correspond to the zero value. See Figure 2 for spatial location of the mooring.

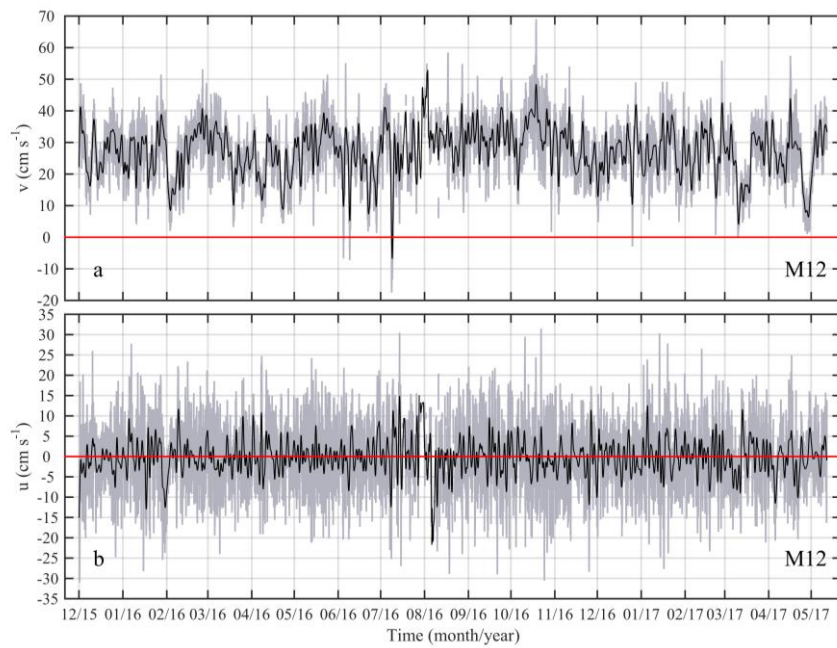


Figure S3. In situ time series of meridional (a) and zonal (b) velocities at M12 (mooring M1, 760 m). Light-gray lines correspond to raw data while black bold lines correspond to 48 h low-pass filtered data. Horizontal red lines correspond to the zero value. See Figure 2 for spatial location of the mooring.

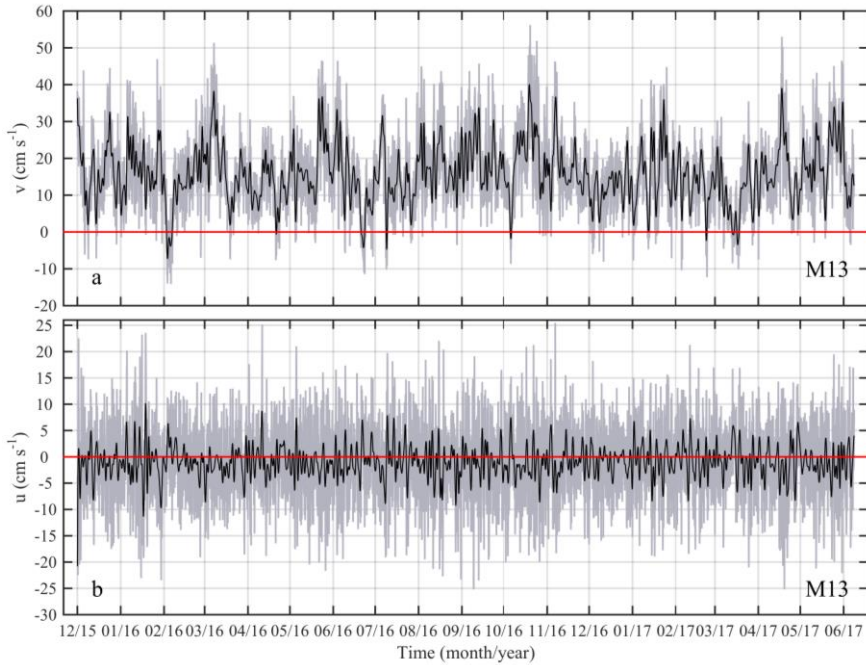


Figure S4. In situ time series of meridional (a) and zonal (b) velocities at M13 (instruments at 1042 m on mooring M1). Light-gray lines correspond to raw data while black bold lines correspond to 48 h low-pass filtered data. Horizontal red lines correspond to the zero value. See Figure 2 for spatial location of the mooring.

1
2
3
4
5
6
7
8
9
10
11
12
13
14
15
16
17
18
19
20
21
22
23
24
25
26
27
28
29
30
31
32
33
34
35
36
37
38
39
40
41
42
43
44
45
46
47
48
49
50
51
52
53
54
55
56
57
58
59
60
61
62
63
64
65

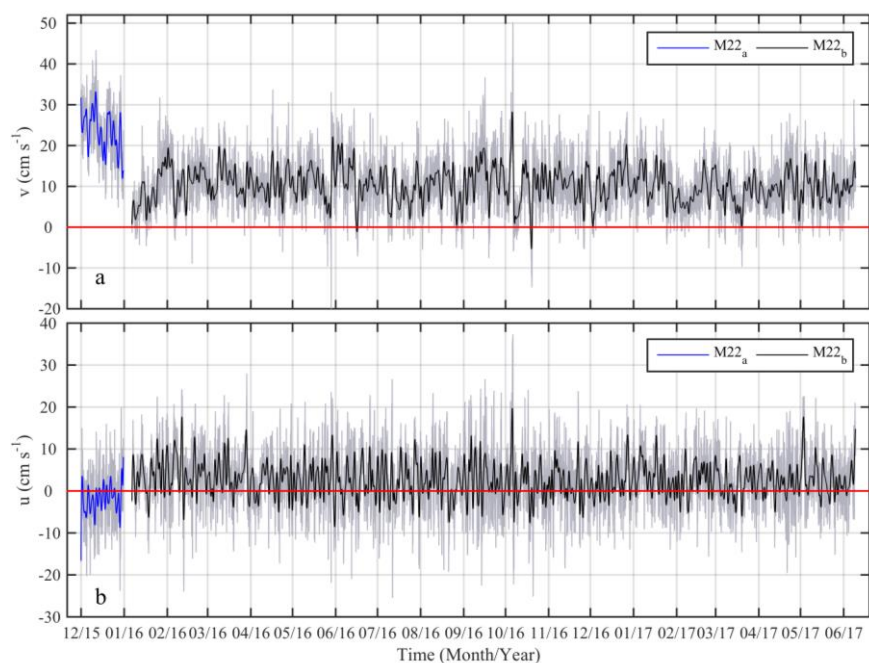


Figure S5. In situ time series of meridional (a) and zonal (b) velocities at M22a (instruments at 1016 m on mooring M2) and at M22b (instruments at 1560 m on mooring M2). Light-gray lines correspond to raw data while bold lines correspond to 48 h low-pass filtered data. Horizontal red lines correspond to the zero value. See Figure 2 for spatial location of the mooring.

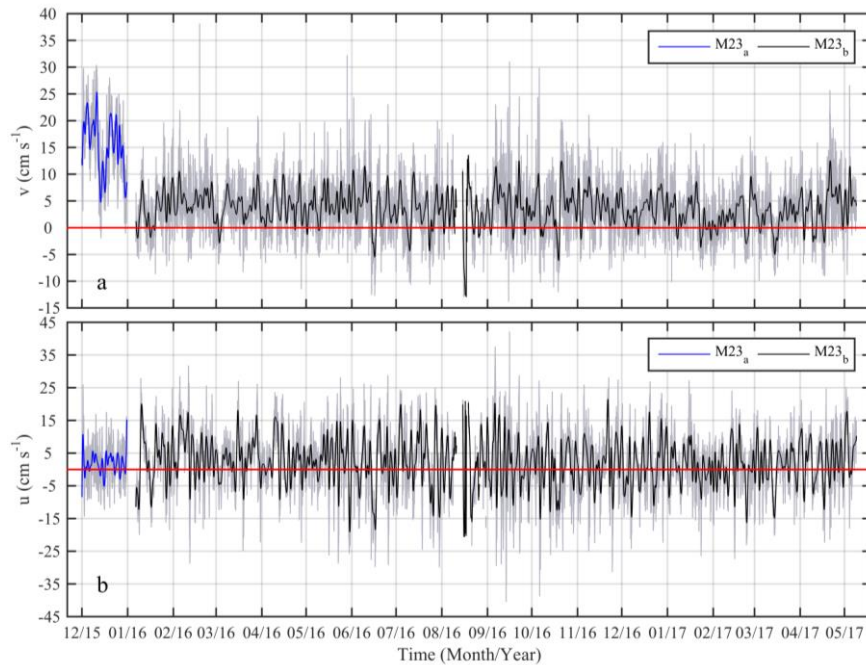


Figure S6. In situ time series of meridional (a) and zonal (b) velocities at M23a (instruments at 1315 m on mooring M2) and at M23b (instruments at 1865 m on mooring M2). Light-gray lines correspond to raw data while bold lines correspond to 48 h low-pass filtered data. Horizontal red lines correspond to the zero value. See Figure 2 for spatial location of the mooring.

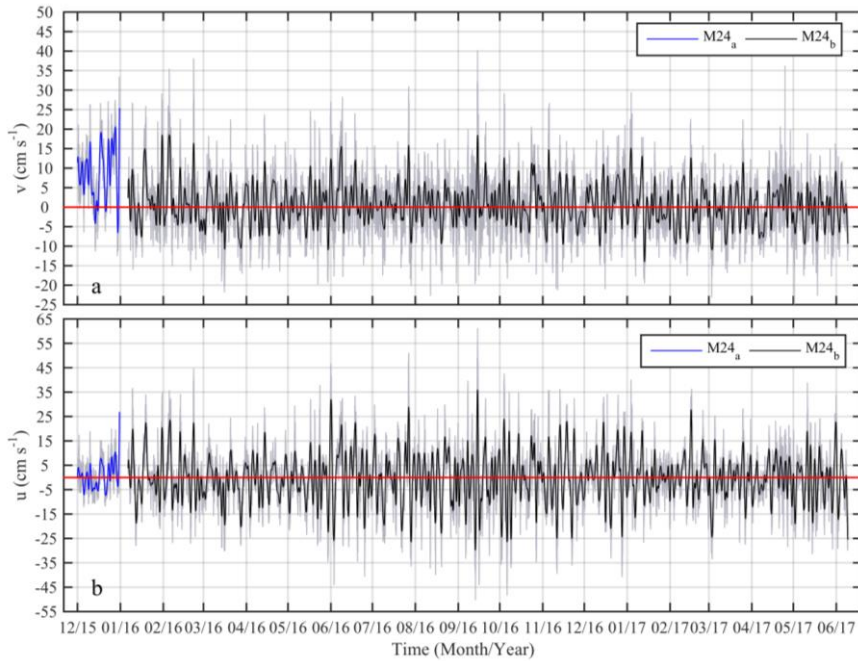


Figure S7. In situ time series of meridional (a) and zonal (b) velocities at M24a (instruments at 1720 m on mooring M2) and at M24b (instruments at 2270 m on mooring M2). Light-gray lines correspond to raw data while bold lines correspond to 48 h low-pass filtered data. Horizontal red lines correspond to the zero value. See Figure 2 for spatial location of the mooring.

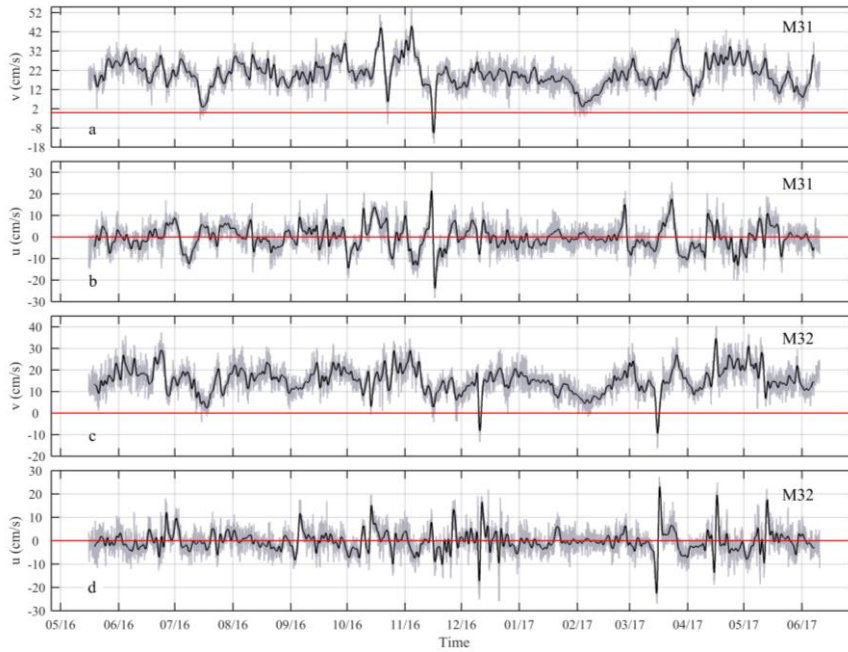


Figure S8. In situ time series of meridional (a) and zonal (b) velocities at M31 (mooring M3, 500 m) and at M32 (c and d; mooring M3, 976 m). Light-gray lines correspond to raw data while black bold lines correspond to 48 h low-pass filtered data. Horizontal red lines correspond to the zero value. See Figure 2 for spatial location of the mooring.

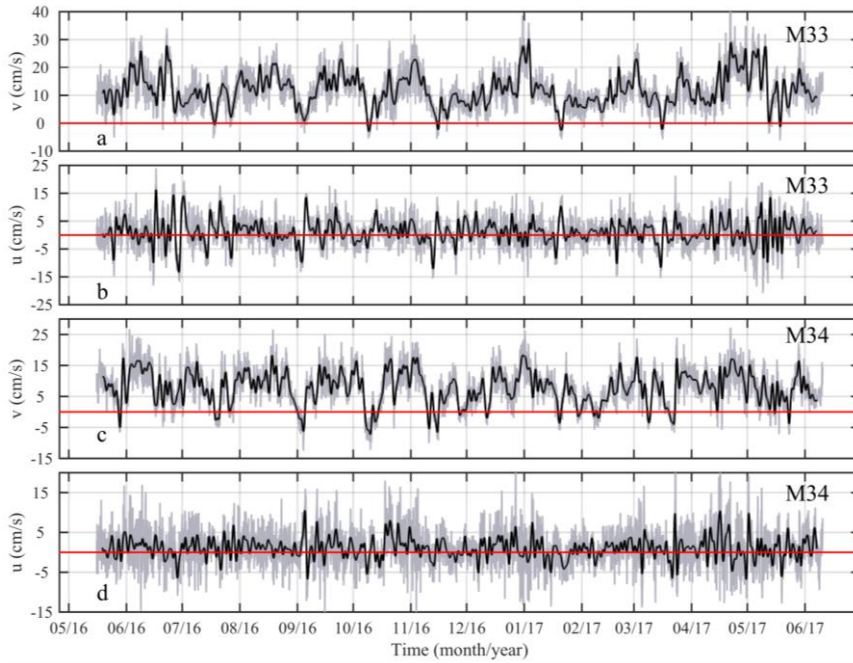


Figure S9. In situ time series meridional (a) and zonal (b) velocities at M33 (mooring M3, 1486 m) and at M34 (c and d; mooring M3, 2100 m). Light-gray lines correspond to raw data while black bold lines correspond to 48 h low-pass filtered data. Horizontal red lines correspond to the zero value. See Figure 2 for spatial location of the mooring.

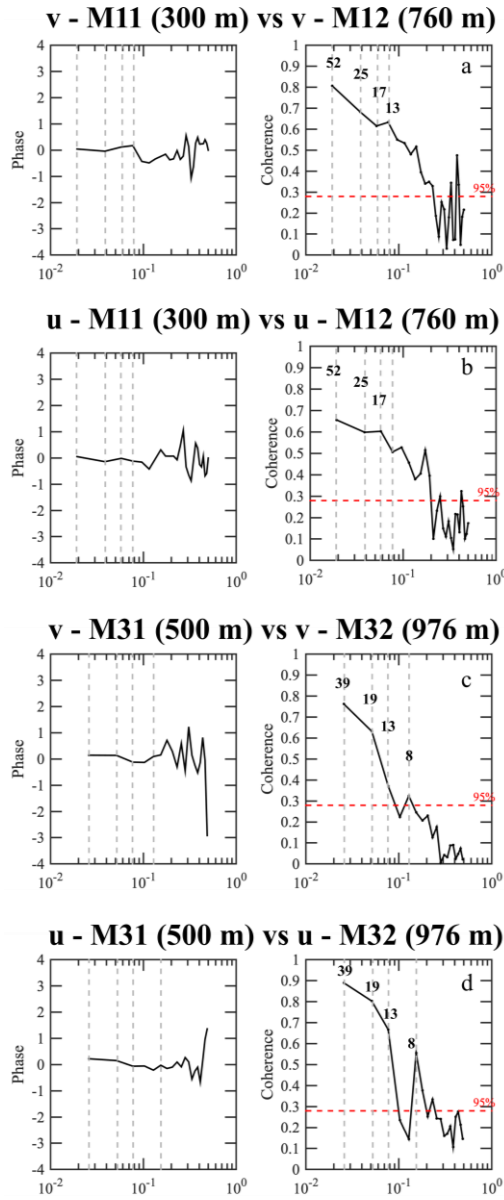


Figure S10. Coherence and phase lag spectra between the meridional and zonal velocities measured in the two uppermost current meters at M1 (a, b) and at M3 (c, d). The horizontal red dashed line in the coherence plots indicated the 95% confidence level.

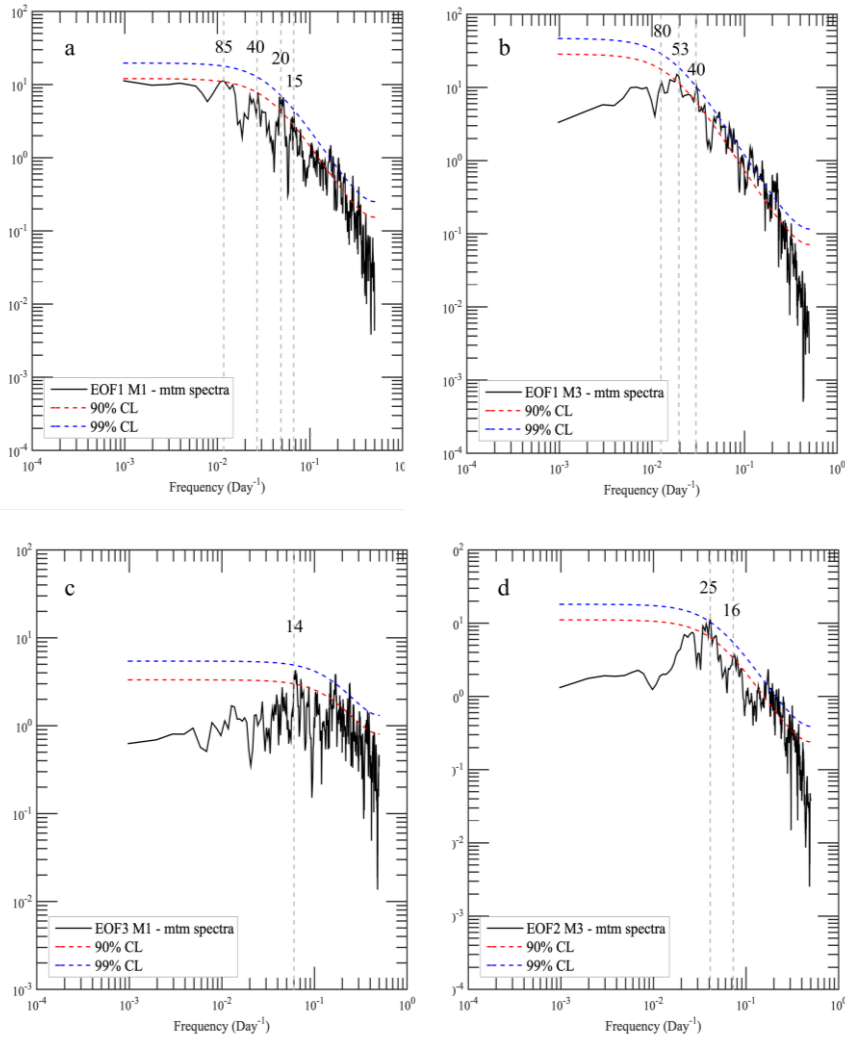


Figure S11. Spectra $(\text{cm/s})^2/\text{day}^{-1}$ of the EOF1 of M1 (a), EOF1 of M3 (b), EOF3 of M1 (c) and EOF2 of M3 (d) time series. The logarithmic scale is applied on both axes. Vertical dashed lines and numbers indicate periodicities in days.

1
2
3
4
5
6
7
8
9
10
11
12
13
14
15
16
17
18
19
20
21
22
23
24
25
26
27
28
29
30
31
32
33
34
35
36
37
38
39
40
41
42
43
44
45
46
47
48
49
50
51
52
53
54
55
56
57
58
59
60
61
62
63
64
65

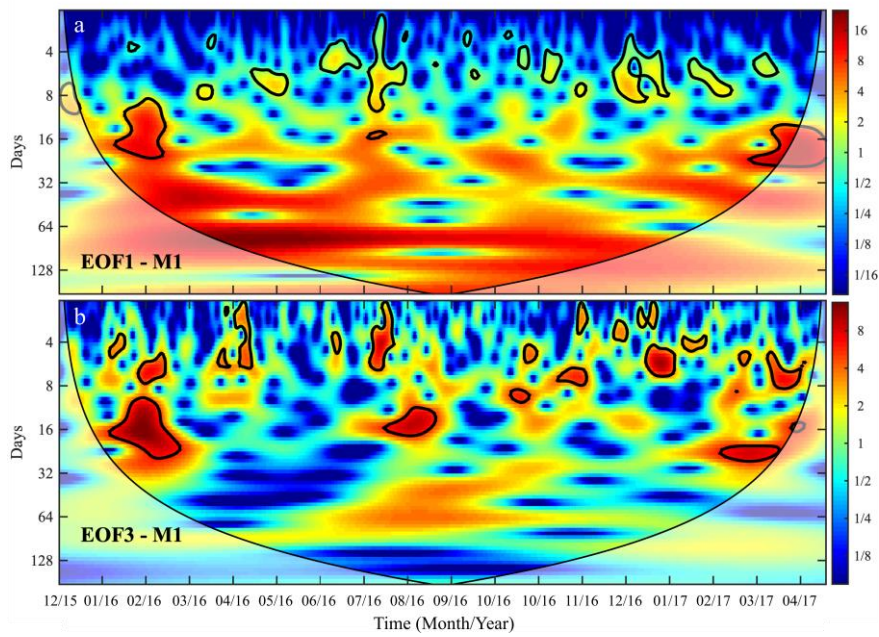


Figure S12. Wavelet power spectrum of (a) EOF1 and (b) EOF3 of M1 standardized time series. The thick black contour designates the 5% significance level against red noise and the cone of influence where edge effects might distort the picture is shown as lighter shade.

1
2
3
4
5
6
7
8
9
10
11
12
13
14
15
16
17
18
19
20
21
22
23
24
25
26
27
28
29
30
31
32
33
34
35
36
37
38
39
40
41
42
43
44
45
46
47
48
49
50
51
52
53
54
55
56
57
58
59
60
61
62
63
64
65

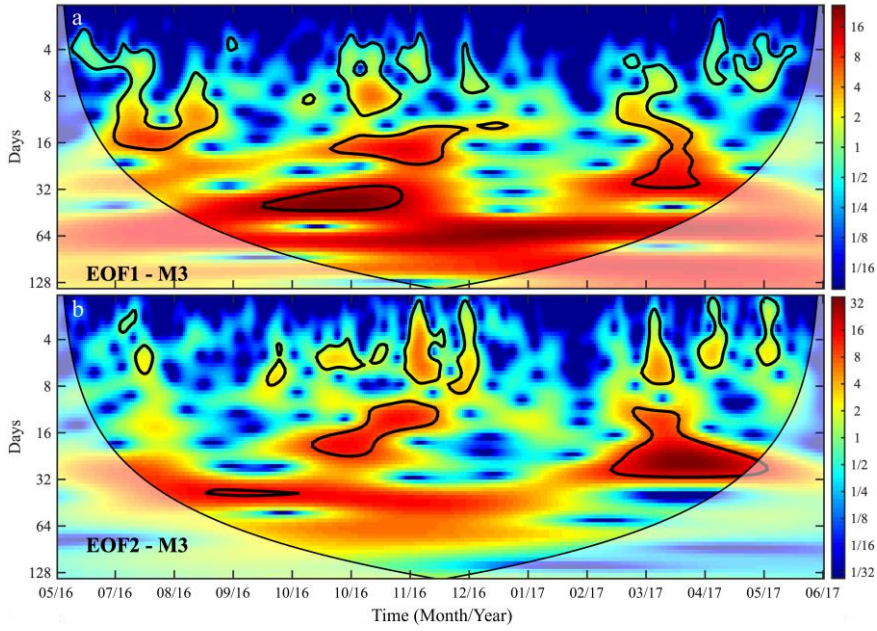


Figure S13. Wavelet power spectrum of (a) EOF1 and (b) EOF2 of M3 standardized time series. The thick black contour designates the 5% significance level against red noise and the cone of influence where edge effects might distort the picture is shown as lighter shade.

1
2
3
4
5
6
7
8
9
10
11
12
13
14
15
16
17
18
19
20
21
22
23
24
25
26
27
28
29
30
31
32
33
34
35
36
37
38
39
40
41
42
43
44
45
46
47
48
49
50
51
52
53
54
55
56
57
58
59
60
61
62
63
64
65

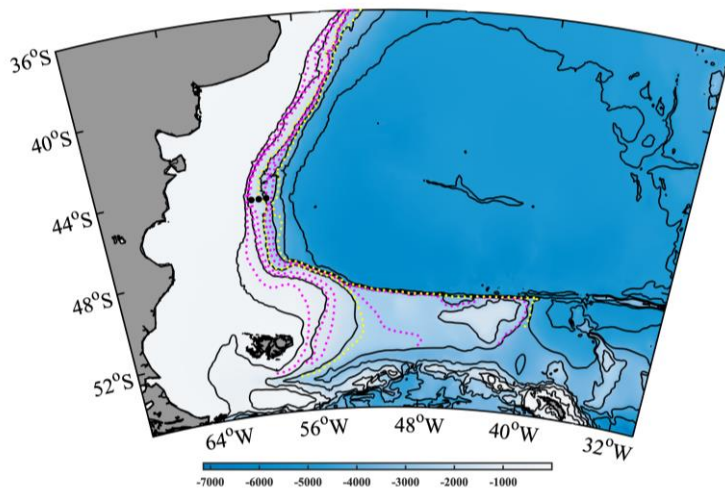


Figure S14. Dotted lines show the PV contours chosen to track the SLA variability. Magenta PV contours correspond from west to east with the following values: $-20 \times 10^{-8} \text{ m}^{-1} \text{ s}^{-1}$, $-10 \times 10^{-8} \text{ m}^{-1} \text{ s}^{-1}$, $-8 \times 10^{-8} \text{ m}^{-1} \text{ s}^{-1}$, $-4.6 \times 10^{-8} \text{ m}^{-1} \text{ s}^{-1}$ and $-4 \times 10^{-8} \text{ m}^{-1} \text{ s}^{-1}$. The yellow dotted lines denote the $-3 \times 10^{-8} \text{ m}^{-1} \text{ s}^{-1}$ and $-5.2 \times 10^{-8} \text{ m}^{-1} \text{ s}^{-1}$ PV contours, selected over the locations of maximum correlation between the along-slope velocities at M11 and M31 and the SLA across the MC at 44.7°S. The black dots indicate the location of the mooring arrays.

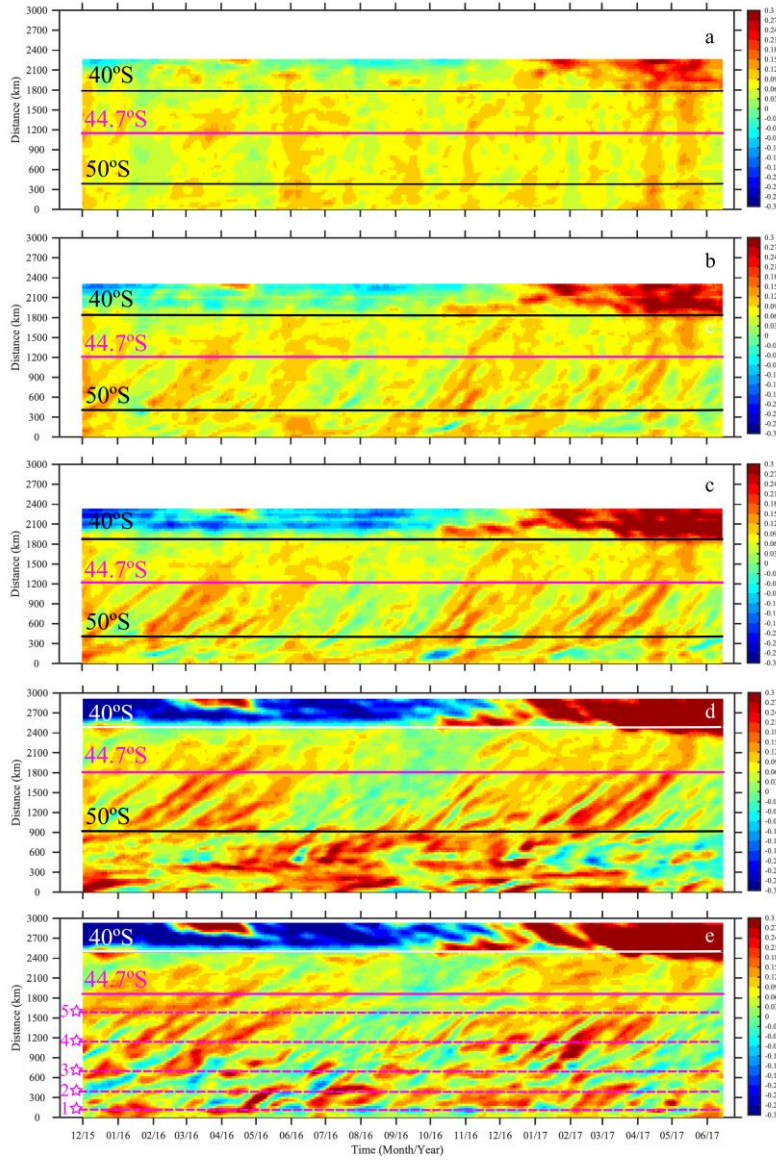


Figure S15. Distance vs time plot of SLA obtained over the following PV lines during CASSIS period: (a) $-20 \cdot 10^{-8} \text{ m}^{-1} \text{ s}^{-1}$, (b) $-10 \cdot 10^{-8} \text{ m}^{-1} \text{ s}^{-1}$, (c) $-8 \cdot 10^{-8} \text{ m}^{-1} \text{ s}^{-1}$, (d) $-4.6 \cdot 10^{-8} \text{ m}^{-1} \text{ s}^{-1}$ and (e) $-4 \cdot 10^{-8} \text{ m}^{-1} \text{ s}^{-1}$. The magenta line indicates the latitude of the mooring's location. The y-axis shows the distance from south to north (in km). The five magenta dashed lines mark the distances from "E1" indicated with stars in Figure 10a.

1
2
3
4
5
6
7
8
9
10
11
12
13
14
15
16
17
18
19
20
21
22
23
24
25
26
27
28
29
30
31
32
33
34
35
36
37
38
39
40
41
42
43
44
45
46
47
48
49
50
51
52
53
54
55
56
57
58
59
60
61
62
63
64
65

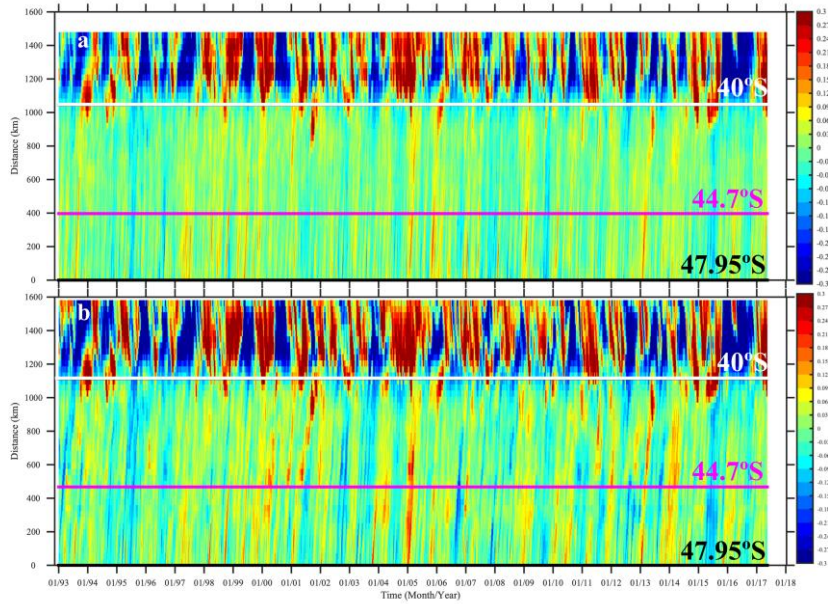


Figure S16. (a) Distance vs time plot of SLA obtained over the potential vorticity contour that goes from W1 to W2 from $\sim 48^{\circ}\text{S}$ indicated in Figure 10a. The magenta line indicates the latitude of the mooring's location. The y-axis shows the distance from north to south (in km). (b) As in (a) but for the potential vorticity contour that goes from E1 to E2 in Figure 10a.

1
2
3
4
5
6
7
8
9
10
11
12
13
14
15
16
17
18
19
20
21
22
23
24
25
26
27
28
29
30
31
32
33
34
35
36
37
38
39
40
41
42
43
44
45
46
47
48
49
50
51
52
53
54
55
56
57
58
59
60
61
62
63
64
65

Formatted: English (United States)